

XXXX

References

- Abarca SF, Montgomery MT, Braun SA, Dunion J. 2016. On the secondary eyewall formation of Hurricane Edouard (2014). *Mon. Weather Rev.*, **144**: 3321-3331.
- Bell MM, Montgomery MT. 2008. Observed structure, evolution, and potential intensity of Category 5 Hurricane Isabel (2003) from 12 to 14 September. *Mon. Weather Rev.*, **65**: 2025-2046.
- Bolton D. 1980. The computation of equivalent potential temperature. *Mon. Weather Rev.*, **108**: 1046-053.
- Braun SA and Coauthors, 2013: NASA's Genesis and Rapid Intensification Processes (GRIP) field experiment. *Bull. Amer. Meteor. Soc.*, **94**: 345-363.
- Braun, SA, Newman PA, Heymsfield GM. 2016. NASA's Hurricane and Severe Storm Sentinel (HS3) investigation. *Bull. Amer. Meteor. Soc.*, **97**: 2085-2102.
- Emanuel KA, 1986. An air-sea interaction theory for tropical cyclones. Part I: steady state maintenance. *J. Atmos. Sci.*, **43**: 585-604.
- Hawkins HF, Rubsam DT. 1968: Hurricane Hilda, 1964. II: Structure and budgets of the hurricane on October 1, 1964. *Mon. Weather Rev.*, **96**: 617-636.

This is the author manuscript accepted for publication and has undergone full peer review but has not been through the copyediting, typesetting, pagination and proofreading process, which may lead to differences between this version and the Version of Record. Please cite this article as doi: [10.1002/qj.3423](https://doi.org/10.1002/qj.3423)

- Hawkins HF, Imbembo SM. 1976. The structure of a small, intense Hurricane Inez 1966. *Mon. Weather Rev.*, **104**: 418-442.
- Kilroy G, Smith RK, Montgomery MT. 2016. Why do model tropical cyclones grow progressively in size and decay in intensity after reaching maturity? *J. Atmos. Sci.*, **73**: 487-503.
- La Seur NE, Hawkins HF. 1963. An analysis of Hurricane Cleo (1958) based on data from research reconnaissance aircraft. *Mon. Weather Rev.*, **91**: 694-709.
- Malkus JS, Riehl H. 1960. On the dynamics and energy transformations in steady-state hurricanes. *Tellus*, **12**: 1-19.
- Marks FD, Black PG, Montgomery MT, Burpee RW. 2008. Structure of the eye and eyewall of Hurricane Hugo (1989). *Mon. Weather Rev.*, **136**: 1237-1259.
- Montgomery MT, Smith RK. 2017. Recent developments in the fluid dynamics of tropical cyclones. *Annu. Rev. Fluid Mech.*, **49**: 1-33.
- Montgomery MT, Bell MM, Aberson SD, Black ML. 2006. Hurricane Isabel (2003): New insights into the physics of intense storms. Part I. Mean vortex structure and maximum intensity estimates. *Bull. Amer. Meteor. Soc.*, **87**: 1335-1347.
- Montgomery MT, Kilroy G, Smith RK, Črnivec N. 2018. Tropical cyclone life cycle in a three-dimensional numerical simulation: Part II: Unbalanced and nonaxisymmetric dynamical processes. *Q. J. R. Meteorol. Soc.*, **144**: submitted.

- Munsell EB, Zhang F, Braun SA, Sippel JA, Didlake AC. 2018. The inner-core temperature structure of Hurricane Edouard (2014): Observations and ensemble variability. *Mon. Weather Rev.*, **91**: 135-155.
- Ooyama K. 1969. Numerical simulation of the life-cycle of tropical cyclones. *J. Atmos. Sci.*, **26**: 3-40.
- Persing J, Montgomery MT, McWilliams J, Smith, RK. 2013. Asymmetric and axisymmetric dynamics of tropical cyclones. *Atmos. Chem. Phys.*, **13**, 12299-12341.
- Rayleigh JWS. 1916. On the dynamics of revolving fluids. *Proc. Roy. Soc. A*, **93**, 148 (also *Sci. Papers*, 6, 447).
- Rotunno R, Emanuel KA. 1987. An air-sea interaction theory for tropical cyclones. Part II Evolutionary study using a nonhydrostatic axisymmetric numerical model. *J. Atmos. Sci.*, **44**: 542-561.
- Smith RK, Montgomery MT. 2013. How important is the isothermal expansion effect to elevating equivalent potential temperature in the hurricane inner-core? *Q. J. R. Meteorol. Soc.*, **138**: 1-5.
- Smith RK, Montgomery MT, Persing J. 2014. On steady-state tropical cyclones. *Q. J. R. Meteorol. Soc.*, **140**: 2638-2649.
- Schmidt C, Smith RK. 2016. Tropical cyclone evolution in a minimal axisymmetric model revisited. *Q. J. R. Meteorol. Soc.*, **142**: 1505-1516.
- Stewart, S. R., 2014: National Hurricane Center Tropical Cyclone Report: Hurricane Edouard (1119 September 2014). Tropical Cyclone Rep. AL062014, National Hurricane

Center, 19pp. Available online at

http://www.nhc.noaa.gov/data/tcr/AL062014_Edouard.pdf.

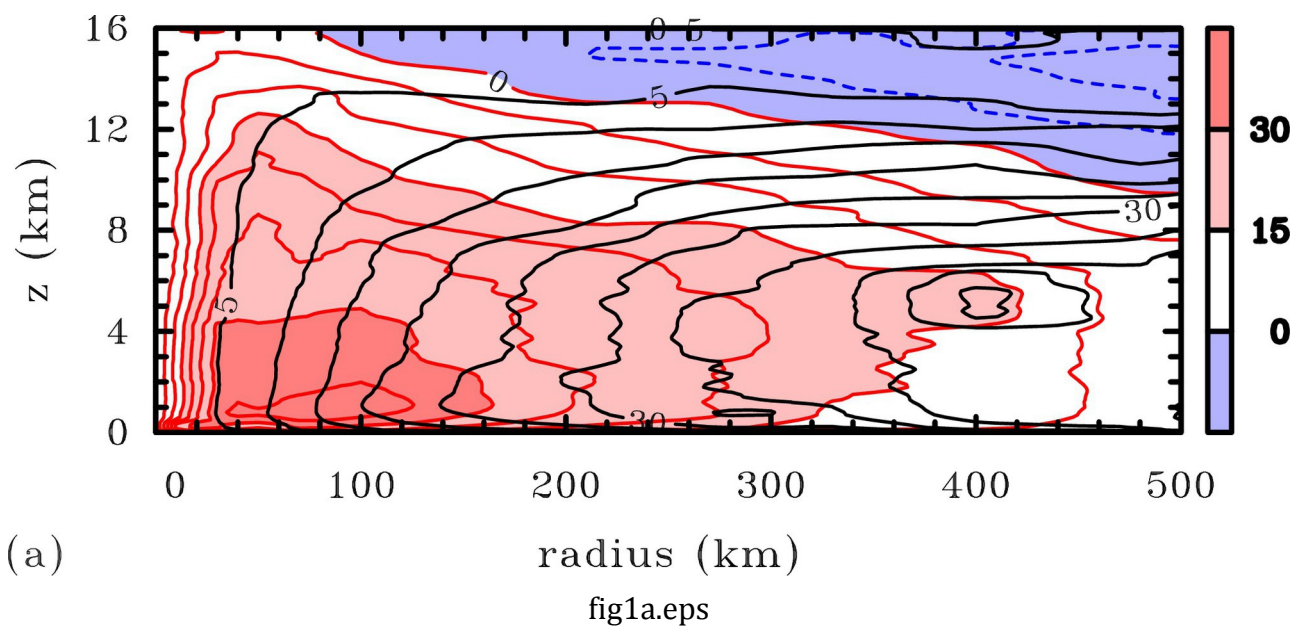
Young K *et al.* 2016. Hurricane and Severe Storm Sentinel (HS3) 2014 Global Hawk Dropsonde Data Analysis Summary.

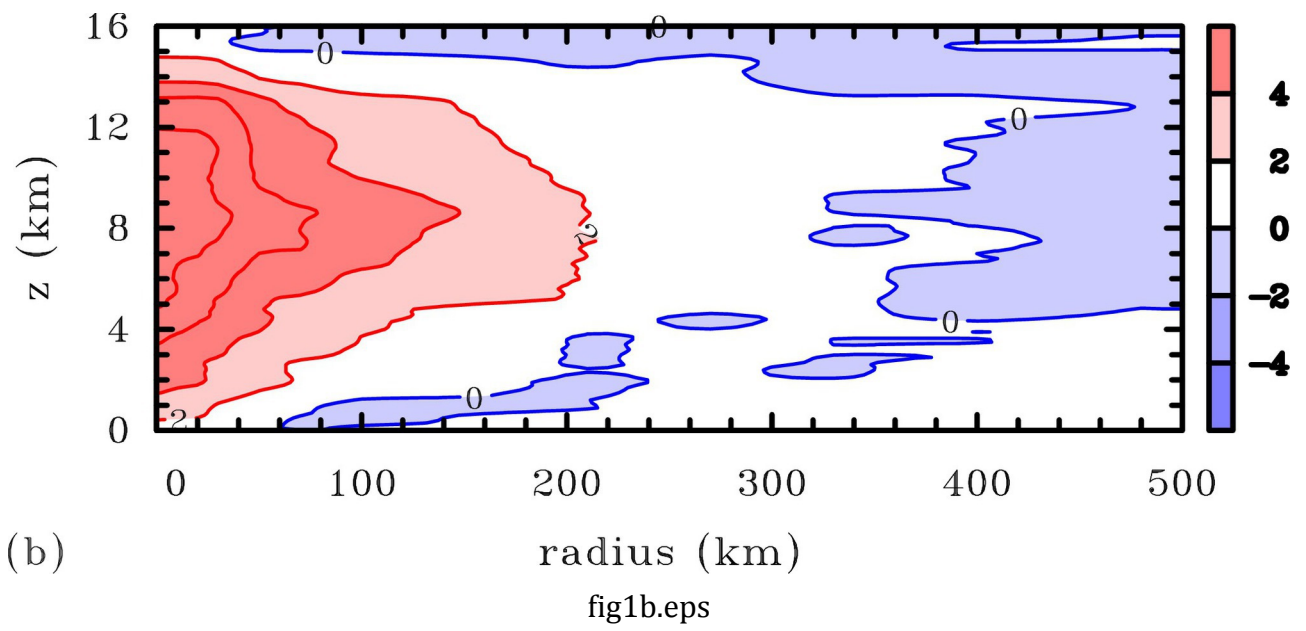
<http://data.eol.ucar.edu/datafile/nph-get/348.004/readme.V3.HS3-2014.GHdropsonde.pdf>

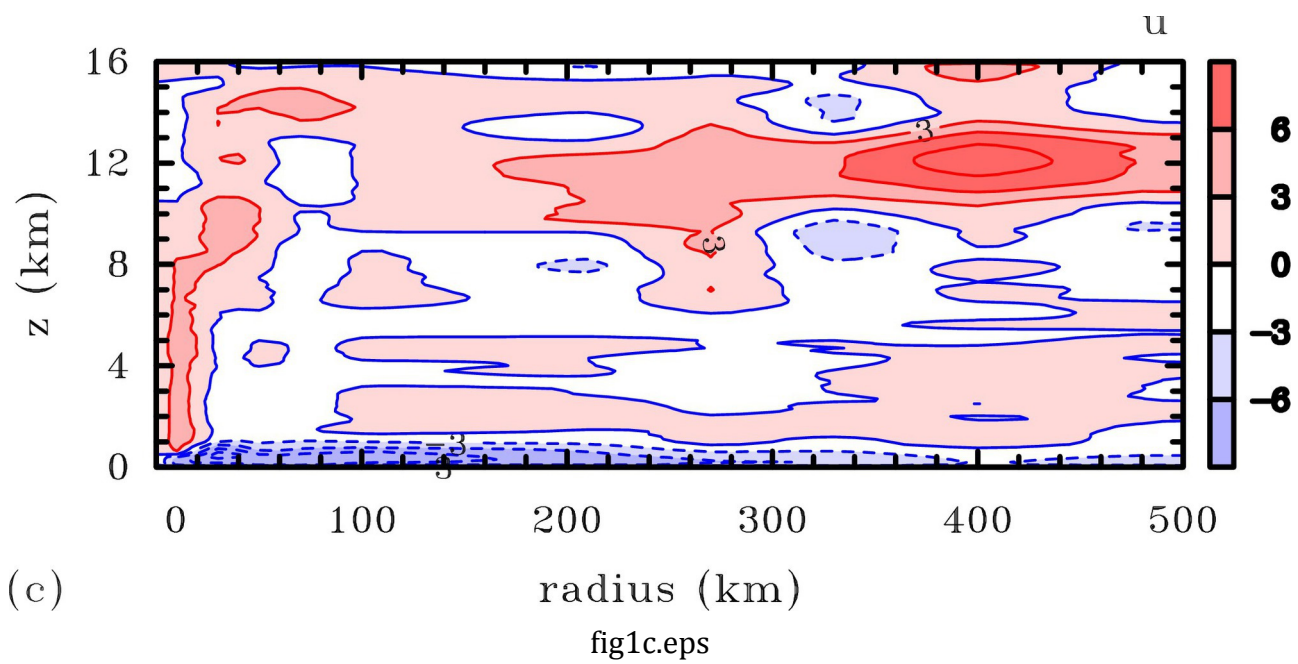
Wick, G., 2015: Hurricane and Severe Storm Sentinel (HS3) Global Hawk AVAPS Dropsonde System. NASA Global Hydrology Resource Center DAAC,

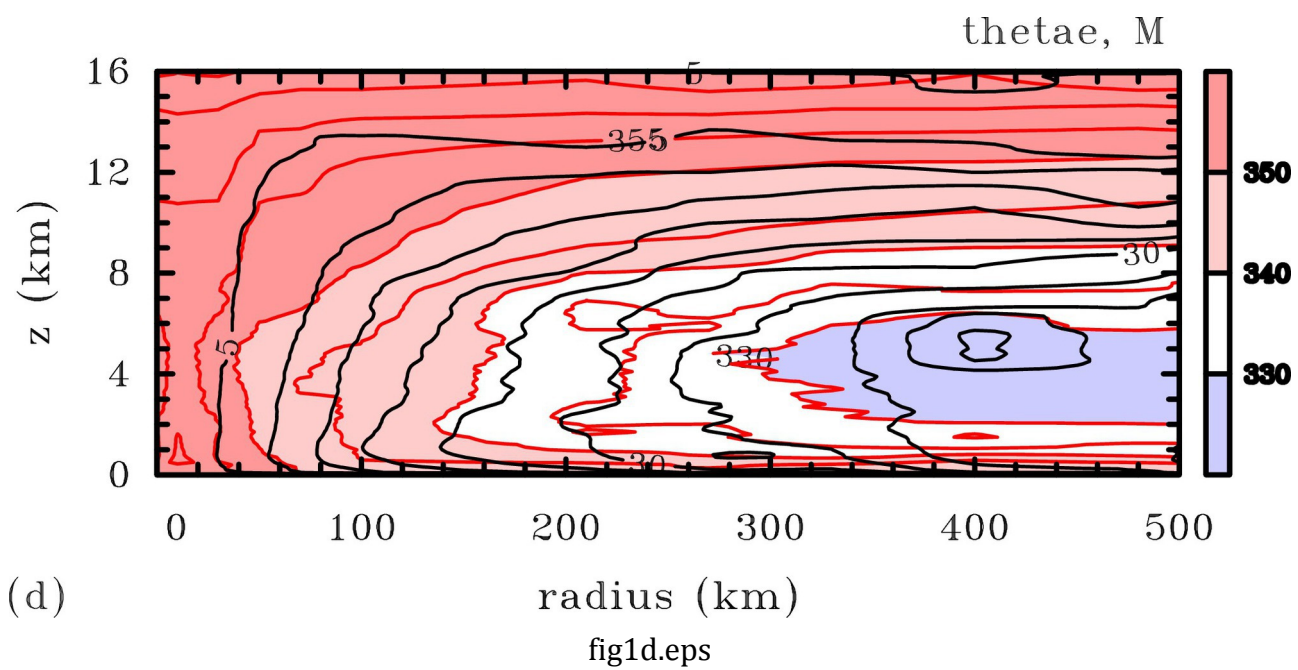
doi:<https://doi.org/10.5067/-HS3/AVAPS/DROPSONDE/DATA201>.

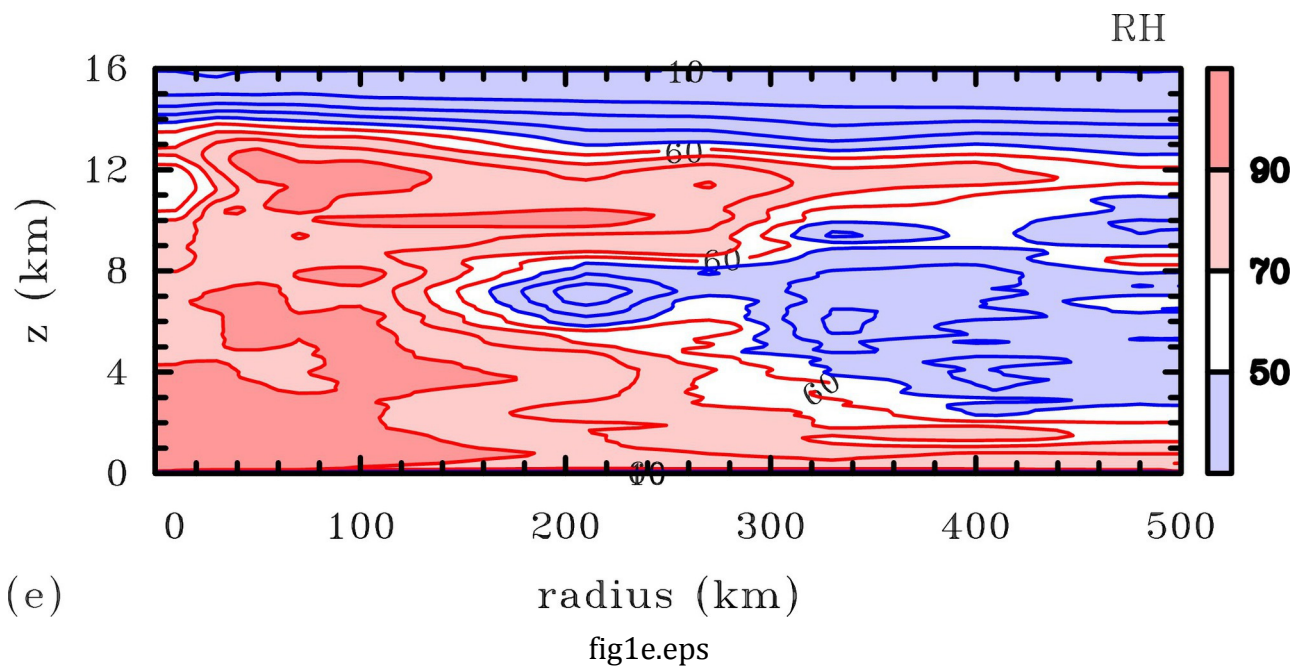
Zawislak J, Jiang H, Alvey GR, Zipser EJ, Rogers RF, Zhang JA, Stevenson SN. 2016. Observations of the structure and evolution of Hurricane Edouard (2014) during intensity change. Part I: Relationship between the thermodynamic structure and precipitation. *Mon. Weather Rev.*, 144: 3333-3354.

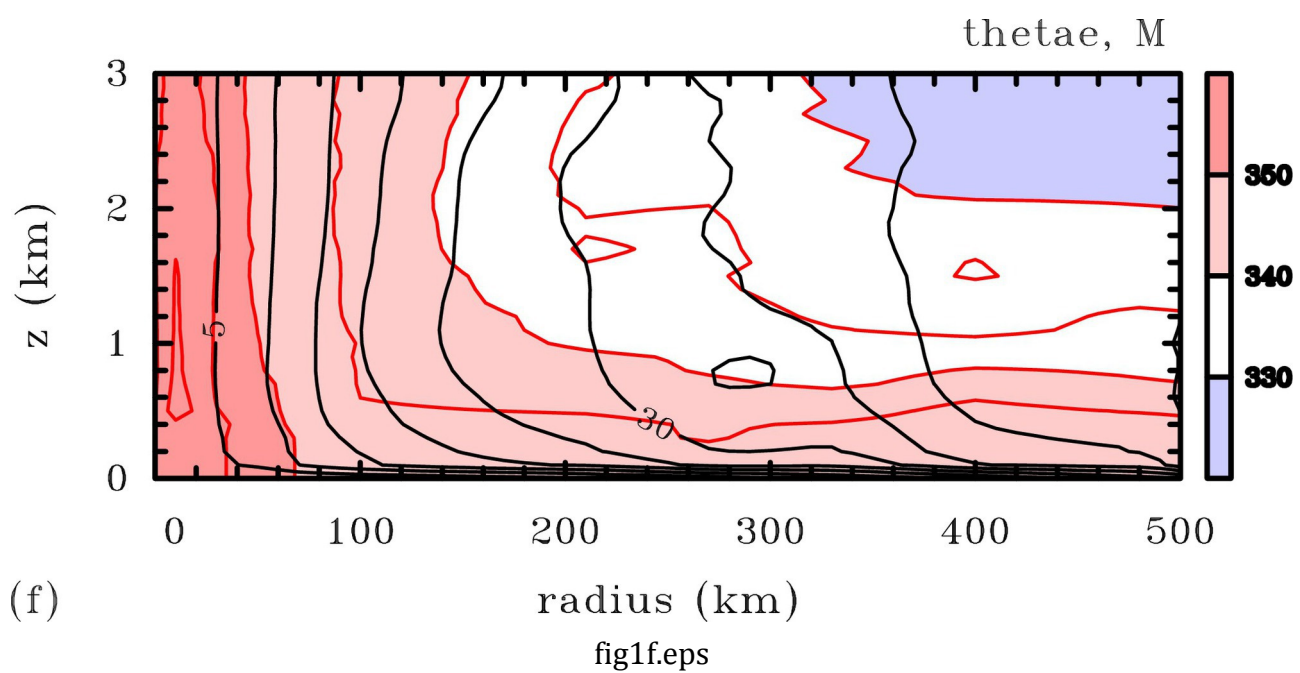














Azimuthally-averaged structure of Hurricane Edouard (2014) just after peak intensity

Roger K. Smith^{a*}, Michael T. Montgomery^b and Scott Braun^c

^a Meteorological Institute, Ludwig Maximilians University of Munich, Munich, Germany

^b Dept. of Meteorology, Naval Postgraduate School, Monterey, CA, USA

^c Laboratory for Mesoscale Atmospheric Processes, NASA Goddard Space Flight Center, Greenbelt, Maryland, MD, USA

*Correspondence to: Prof. Roger K. Smith, Meteorological Institute, Ludwig-Maximilians University of Munich, Theresienstr. 37, 80333 Munich, Germany. E-mail: roger.smith@lmu.de

Analyses of dropsonde data just after the mature stage of Hurricane Edouard (2014) are presented. These data, which have unprecedentedly high spatial resolution, were obtained by the unmanned NASA Global Hawk during the Hurricane and Severe Storm Sentinel (HS3) field campaign. The analyses are related to theories of tropical cyclone structure and behaviour. In particular, the findings highlight the radial outflow above the boundary layer below about 8 km and between about 80 km and 220 km radius. This radial outflow would explain the observed spin down of the storm according to the classical mechanism. The findings highlight also a limitation of the assumed steadiness of the storm over the period of data collection.

Key Words: Tropical cyclone, hurricane, observed structure and behaviour

Received October 17, 2018; Revised ; Accepted

1. Introduction

In the past there have been few measurements of hurricane structure through the depth of the troposphere, the reason being that most aircraft reconnaissance flights have not been able to sample the upper troposphere. Some classic observational studies are those of La Seur and Hawkins (1963), Hawkins and Rubsam (1968) and Hawkins and Imbembo (1976) to whom *in situ* data from an instrumented high-flying jet aircraft were available. The situation changed recently through the deployment of the NASA* Global Hawk, an unmanned drone capable of releasing dropsondes in rapid succession from the lower stratosphere. During NASA's Hurricane and Severe Storm Sentinel (HS3; Braun *et al.* 2016) field campaign in 2014, comparatively high temporal and spatial resolution dropsonde observations were made over the Atlantic Ocean in Hurricane Edouard during four missions between 11 to 19 September 2014. A map showing the location of each dropsonde is contained in Figure 1 of Zawislak *et al.* (2016), while a description of the storm during its lifetime is given by Stewart (2014). Brief descriptions of the storm and the missions flown was given by Braun *et al.* (2016) and Munsell *et al.* (2018).

The structure of Edouard was particularly well sampled on 16–17 September while it was near peak intensity. On this mission, which lasted about 23 h, 87 dropsondes were deployed into the hurricane from a height of 18 km. The purpose of this paper is to present azimuthally averaged, radius-height cross sections of various quantities obtained from analyses of these unique data and to compare these analyses with theories of tropical cyclone behaviour.

2. Data

The 87 dropsondes were released into Edouard between 15:06 UTC 16 September and 08:28 UTC 17 September 2014 during which time the storm moved from about 32°N to 35°N (Stewart 2014, Table 1). The distribution of the dropsondes is shown in Abarca *et al.* (2016, Figure 2(a)). The sonde data were post-processed by NCAR using their Atmospheric Sounding Processing Environment (ASPEN) software (Young *et al.* 2016), see Wick *et al.* (2015). The original analyses of the dropsondes did not include a dry bias correction in the upper troposphere, but the present ones have used the correct humidity values. The analysis of these sondes is described briefly below.

*National Atmospheric and Space Administration

36 2.1. Computation of azimuthal averages

37 To calculate the azimuthal averages, the dropsonde data were first interpolated to 181 pressure levels with a spacing of 5 mb. The storm
38 centre positions over the time period of the flight were used to determine the location of each dropsonde relative to the evolving centre
39 position. The National Hurricane Center best track data were used also to estimate the mean storm motion over the flight period. The
40 positions of the dropsonde data were shifted to a reference time of 00 UTC 17 September using the storm motion and the time difference
41 between the sonde time and this reference time. Here, the sonde time is the time of the actual measurement at a particular level. Using
42 these adjusted positions relative to the centre, radial and tangential velocities were calculated with the storm motion removed to obtain
43 storm-relative flow. This analysis was done for all dropsondes during the flight. Bins were then created for averaging after all derived
44 fields such as radial and tangential velocity were calculated.

45 The midpoints of the bins were at radial locations 10, 35, 70, 110, 170, 245, 320, 400, 480 and 560 km from the centre[†]. The number
46 of soundings were distributed within each bin as follows: 0-20 km radius (10 sondes), 20-40 km (9), 40-60 km (7), 60-90 km (10),
47 90-120 km (8), 120-200 km (3), 200-280 km (14), 280-360 km (9), 360-440 km (8), 440-520 km (8), 520-600 km (7). No additional
48 smoothing was applied to the individual dropsonde data. If, when computing the azimuthal mean, some values were missing from
49 individual soundings, they were simply not included in the calculation of the mean. For the height-radius coordinate used in the plots
50 to be shown, there were no missing azimuthal mean values.

51 2.2. Steady-state composite data

52 Although the storm was at peak intensity near the start of measurements, the intensity decreased by about 10 m s^{-1} during the period
53 of measurements (see Abarca *et al.* 2016, Figure 1 and accompanying discussion of the various factors in this decay). Attempts were
54 made to subdivide the data into two separate subsets, one in the first half of the flight and another in the second half. The number of
55 soundings were distributed as follows over the course of the first half of the flight, and the second half of the flight: radius 0-20 km
56 (first half 6, second half 4), 20-40 km (4, 5), 40-60 km (5, 3), 60-90 km (4, 7), 90-120 km (4, 4), 120-200 km (2, 1), 200-280 km (6,
57 8), 280-360 km (3, 6), 360-440 km (3, 5), 440-520 km (3, 5), 520-600 km (2, 5). Clearly, breaking up the soundings into two separate
58 halves of the flight reduces the number of samples in each radial bin, although not necessarily by half since a good part of the first half
59 of the flight was sampling storm outflow beyond 600 km radius. The biggest problem occurs in the 120-200 km radius bin, where the
60 second half of the flight has only one sounding, and much of that data is missing, so contours cannot be drawn there. For these reasons,
61 and because there was qualitative similarity between the derived structures from the two data sets in regions where there was data, we
62 have based the analysis below on a composite for the whole period. Thus, all the storm-relative dropsonde data from the whole flight
63 occurring within a particular bin were averaged. This procedure is tantamount to assuming the storm to be in a steady state for the
64 duration of the flight. Some limitations of the steady state assumption will emerge later.

65 3. Storm structure

66 Figure 1 shows radius-height cross sections obtained from the dropsonde data as described in subsection 2.1 above. The data are slightly
67 smoothed using a centred 1-4-1 box filter applied 10 times.

68 3.1. Tangential wind and warm core structure

69 The storm-relative composite tangential wind component (v , Figure 1a) and temperature perturbation (dT , panel (b)) show the classical
70 structure of a warm-cored vortex with the maximum wind in the lower troposphere and the wind decreasing with height, becoming
71 anticyclonic in the upper troposphere. The decrease in the tangential velocity component with height corresponds through balance
72 considerations with the warm-core structure (see Figure 1b)

73 There is evidence of a secondary tangential wind maximum at a radius of about 100 km, the inner maximum being near 50 km
74 radius. The formation of this secondary wind maximum was the focus of a separate study (Abarca *et al.* 2016, see below for more).
75 The upper-level anticyclone begins at a radius of about 80 km, while the strength of the anticyclone increases with radius and the
76 anticyclonic circulation deepens with increasing radius. The maximum anticyclonic flow is found at an altitude between 14 and 15 km.

77 Figure 1(a) shows also the absolute angular momentum (or M -) surfaces corresponding with the tangential wind component. These
78 are calculated using the formula $M = rv + \frac{1}{2}fr^2$, where r is the radius and f is the Coriolis parameter at the mean latitude of Edouard
79 (33 N) during the period of dropsonde measurements. Consistent with theoretical expectations, the M -surfaces flare outwards with
80 height, with M mostly increasing with radius and decreasing with height. There is an elevated local maximum of M located at a height
81 of about 5.5 km and a radius of about 410 km and two additional maxima at larger radii. These maxima are accompanied by a negative
82 radial gradient of M at radii beyond them, implying that the flow is inertially unstable. Since the dropsonde data at these radii are rather
83 sparse (see Abarca *et al.* 2016, Figure 2(b)) and the period of collection spans an interval of more than 16 h, we do not attribute much
84 significance to the implied regions of instability at these radii.

85 There is a marked positive temperature anomaly inside a radius varying between 100-150 km, depending on height (Figure 1(b)).
86 (For the calculation of temperature perturbation, the “environmental temperature” was determined by averaging all dropsonde data at
87 radii > 200 km. Specifically, there were 46 soundings used in calculation of the “environmental” mean temperature for the temperature
88 perturbation plot.) The temperature anomaly has a maximum of nearly 10°C at an altitude of about 8 km close to the axis of rotation.
89 There is a weak cold temperature anomaly at low levels beyond about 50 km radius. The negative temperature anomalies beyond about
90 400 km are due to the way the ambient temperature has been defined (see section 2.1). Since the reference temperature is based on an
91 average of all soundings beyond a radius of 200 km and if the temperature in this region decreases outwards, negative anomalies would
92 be expected at large radii. The low-level negative anomaly between 100 and 300 km radius is presumably a result of the evaporation of
93 falling raindrops.

[†]The data set is the same as that used by Abarca *et al.* (2016). However, the subdivision into bins is somewhat different. Even so, the tangential wind field in Abarca *et al.* (Figure 3(a)) is very similar to that shown in Figure 1(a). The pressure field is rather smooth and should be similar between the two analyses. Indeed, Abarca *et al.* did note that “the data were robust to different bin-length choices”.

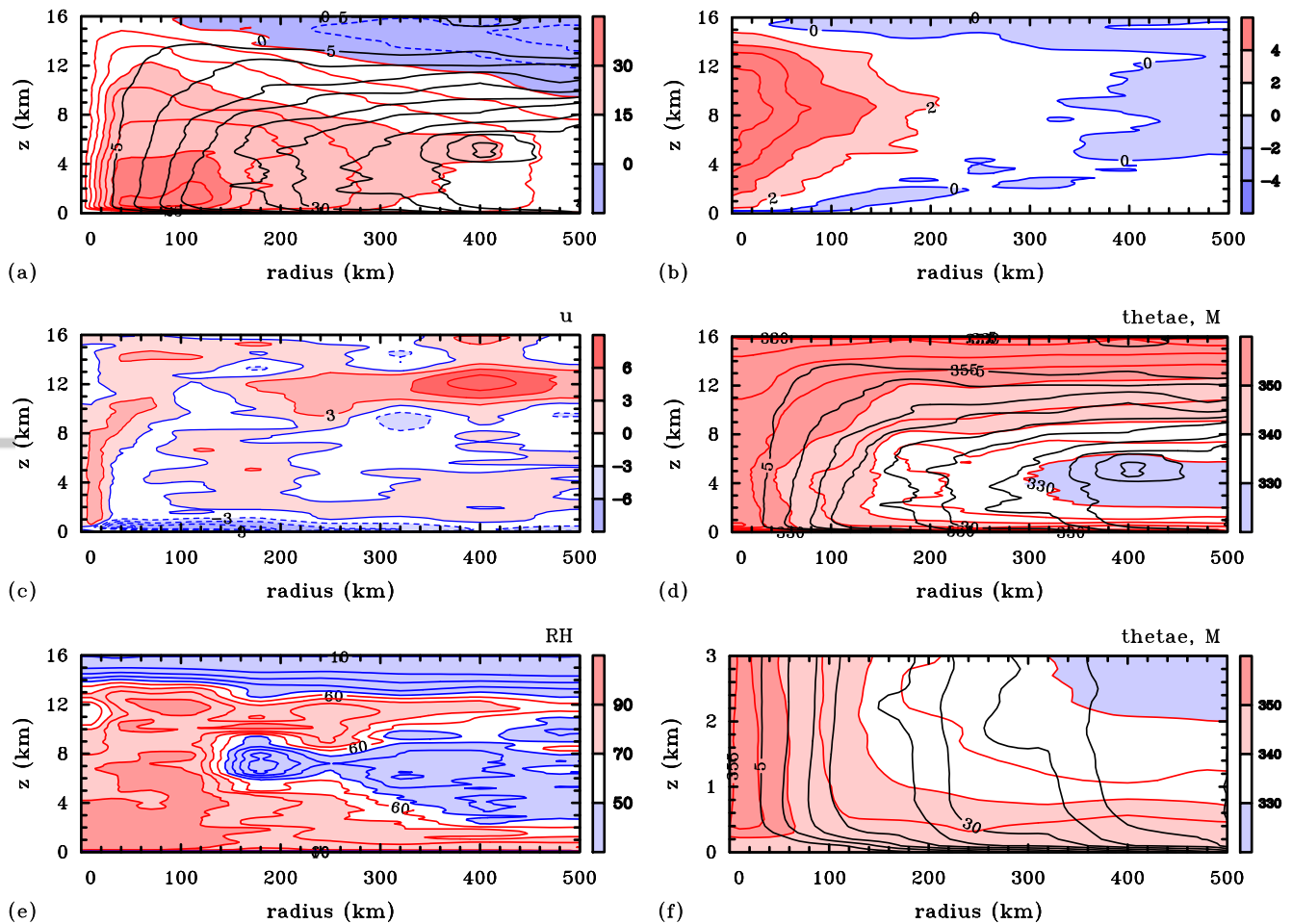


Figure 1. Radius-height cross sections of selected fields derived from the dropsonde data: (a) tangential velocity component, contour interval 5 m s^{-1} , shading indicated on the side bar in m s^{-1} , and absolute angular momentum, black lines, contour interval $5 \times 10^5 \text{ m}^2 \text{ s}^{-1}$; (b) temperature perturbation, contour interval 2 K (positive values), 1 K (negative values), shading indicated on the side bar in K; (c) radial velocity component, contour interval 3 m s^{-1} , shading indicated on the side bar in m s^{-1} ; (d) equivalent potential temperature, contour interval 10 K, shading indicated on the side bar in K, and absolute angular momentum, black lines, contours as in (a); (e) relative humidity, contour interval 10%, shading indicated on the side bar in %; (f) a zoomed in version of panel (d) at heights below 3 km.

94 3.2. Radial velocity component

95 The storm-relative composite radial flow (u , Figure 1c) shows two features of the classical tropical cyclone structure with a layer of
 96 strong inflow below about 1 km extending to large radii as well as a layer of strong outflow in the upper troposphere between about 9
 97 and 14 km depending on radius. The maximum low-level inflow is about 15 m s^{-1} . The layer of upper tropospheric outflow is a few
 98 km deep with a maximum of nearly 12 m s^{-1} at about 12 km altitude and 400 km radius.

99 Perhaps surprisingly, the layers of anticyclonic flow and outflow in the upper troposphere have only a small overlap and mainly at
 100 large radii. In particular, the level of maximum outflow does not coincide with that of the maximum anticyclonic flow, which is typically
 101 2 km higher. A plausible explanation is that during the earlier part of the period of investigation, the outflow was higher than during
 102 the later part. This possibility is supported by the fact that the region of strong outflow begins beyond 100 km radius near where the
 103 secondary wind maximum and secondary eyewall have formed (cf. Abarca *et al.* 2016). In the region inside a radius of 100 km, there
 104 is a localized region of outflow with a maximum near 14 km height, presumably remnants of the previous outflow at a higher level.
 105 **The foregoing difficulty in reconciling the radial and tangential structure of the storm highlights a potential limitation of assuming that
 106 the storm is in a quasi-steady state for the purpose of the analysis.**

107 Another interesting feature of the radial flow is the broad region of outflow inside a radius of about 220 km in the lower half of the
 108 troposphere above the shallow surface-based boundary layer inflow. This outflow has two local maxima, the inner one associated in
 109 part with the inner eyewall and the outer one with the secondary eyewall and secondary wind maximum as documented in Abarca *et al.*
 110 (2016). This pattern of outflow would suggest that the flow in these regions is spinning down by the outward radial advection of
 111 the M -surfaces. However, this spin down effect would be countered by the vertical advection of air with high values of M from the
 112 boundary layer. It was shown by Abarca *et al.* (2016, see their Figure 4b), that the boundary layer flow was supergradient below both
 113 the primary and secondary eyewalls on the day prior to the present observations. The fact that the storm had just begun to weaken (see
 114 section 2.1) would indicate that the spin down tendency due to the outward radial advection of the M -surfaces would be dominant,
 115 at least for the primary eyewall. The role of the vertical advection of supergradient values of M from the boundary layer to spin up
 116 the primary eyewall was highlighted by the study of Schmidt and Smith (2016) using a minimal three-layer numerical model and was
 117 discussed in a more general context by Montgomery and Smith (2017: section 3.9).

118 **Beyond the 220 km radius in Figure 1c, there are alternate layers of inflow and outflow with outflow being the dominant feature
 119 between about 1.5 km and up to 5 km in height.**

120 Other interesting features of the radial flow are the layers of inflow in the upper troposphere, above and below the outflow layer.
 121 Such features are often seen in numerical model simulations, but to our knowledge are not well understood.

122 3.3. Pseudo-equivalent potential temperature

123 The distribution of pseudo-equivalent potential temperature[‡], θ_e , (Figure 1d and 1f) shows the classical structure also. (Figure 1f is a
 124 zoomed in plot of Figure 1d in the lowest 3 km.) Principal features are: the mid-tropospheric minimum beyond a radius of about 100
 125 km, increasing in prominence with radius; the tendency for the isopleths of θ_e to become close to vertical in the lower troposphere
 126 inside a radius of 100 km; and the tendency for the isopleths of θ_e to slope outwards and become close to horizontal in the upper
 127 tropospheric outflow layer. There is an approximate congruence between the θ_e - and M -surfaces in the inner core region and in the
 128 upper troposphere (the M -surfaces are shown also in Figure 1d and 1f). This approximate congruence in the inner-core region ($r < 200$
 129 km) forms the cornerstone of the steady-state axisymmetric hurricane model by Emanuel (1986).

130 Throughout much of the troposphere, θ_e has a negative radial gradient. This is, in part, a reflection of the structure in the boundary
 131 layer. In this layer (below 1 km) the negative radial gradient of θ_e is apparent only inside a radius of about 100 km and is a result
 132 of the presumed increase in surface moisture flux with decreasing radius (Malkus and Riehl 1960, Ooyama 1969). Such a localized
 133 gradient was documented in the classical observational analysis of Hawkins and Imbembo (1976) and has been confirmed by more
 134 recent work (Montgomery *et al.* 2006, Marks *et al.* 2008, Bell and Montgomery 2008, Smith and Montgomery 2013). Maximum values
 135 of θ_e exceed 355 K in the low to mid troposphere near and inside the eyewall region. The surface value is approximately constant at
 136 350 K outside of 100 km radius. The minimum value in the mid to low troposphere falls to values less than 320 K beyond about 300
 137 km radius (the region highlighted in blue in Figure 1d).

138 3.4. Relative humidity

139 Values of relative humidity[§], (RH , panel(d)), exceed 90% inside a radius of 200 km and below about 7 km altitude. At larger radii,
 140 values are high ($> 80\%$) in a shallow near-surface layer, but decrease markedly with height with values of less than 50% through much
 141 of the troposphere, especially beyond about 300 km in radius. These low values are an indication of drying in the subsiding branch of
 142 the secondary circulation. This plot does indicate a couple of features of interest. First, the RH starts to drop off beyond the secondary
 143 wind maximum, perhaps suggesting that this wind maximum either forms near the boundary with dry air or acts as a potential barrier
 144 to dry air. Second, very dry air is being drawn inwards just below the outflow layer.

145 4. Conclusions

146 In this paper we have used a dropsonde data set with unprecedentedly high spatial coverage from the NASA HS3 experiment to analyze
 147 the azimuthally-averaged structure of Hurricane Edouard (2014) just after its peak intensity. The dropsondes were deployed from above
 148 the tropopause and enable a sampling of the full troposphere. The analyses of these unique observations confirm many known structural
 149 features of a mature tropical cyclone, e.g. tangential wind structure, radial wind structure, warm core structure and equivalent potential
 150 temperature structure. In particular, they show radial outflow above the boundary layer in the lower half of the troposphere and inside
 151 about 220 km radius, which would explain the observed spin down of the storm as absolute angular momentum surfaces are advected
 152 outwards. Nevertheless, even with such an unprecedentedly high density of dropsondes to estimate the azimuthally-averaged structure,
 153 there remains an issue in reconciling the radial and tangential structure of the hurricane. This issue appears to arise from the analysis
 154 assumption of a quasi-steady state during the period of observations, an assumption that stands out as an important limitation of any
 155 analysis of dropsonde data over such an extended period of observations as the one in this case.

156 5. Acknowledgements

157 We thank Jun Zhang and two anonymous reviewers for their perceptive and constructive comments on the original manuscript. RKS
 158 acknowledges financial support for tropical cyclone research from the Office of Naval Research Global under Grant No. N62909-15-
 159 1-N021. MTM acknowledges the support of NSF grant AGS-1313948, NOAA HFIP grant N0017315WR00048, NASA (HS3) grant
 160 NNG11PK021, ONR grant N0001417WX00336, and the U. S. Naval Postgraduate School.

161 6. References

- 162 Abarca SF, Montgomery MT, Braun SA, Dunion J. 2016. On the secondary eyewall formation of Hurricane Edouard (2014). *Mon. Weather Rev.*, **144**:
 163 3321-3331.
 164 Bell MM, Montgomery MT. 2008. Observed structure, evolution, and potential intensity of Category 5 Hurricane Isabel (2003) from 12 to 14
 165 September. *Mon. Weather Rev.*, **65**: 2025-2046.
 166 Bolton D. 1980. The computation of equivalent potential temperature. *Mon. Weather Rev.*, **108**: 1046-053.
 167 Braun SA and Coauthors, 2013: NASAs Genesis and Rapid Intensification Processes (GRIP) field experiment. *Bull. Amer. Meteor. Soc.*, **94**: 345-363.
 168 Braun, SA, Newman PA, Heymsfield GM. 2016. NASAs Hurricane and Severe Storm Sentinel (HS3) investigation. *Bull. Amer. Meteor. Soc.*, **97**:
 169 2085-2102.
 170 Emanuel KA, 1986. An air-sea interaction theory for tropical cyclones. Part I: steady state maintenance. *J. Atmos. Sci.*, **43**: 585-604.
 171 Hawkins HF, Rubsam DT. 1968: Hurricane Hilda, 1964. II: Structure and budgets of the hurricane on October 1, 1964. *Mon. Weather Rev.*, **96**:
 172 617-636.
 173 Hawkins HF, Imbembo SM. 1976. The structure of a small, intense Hurricane Inez 1966. *Mon. Weather Rev.*, **104**: 418-442.
 174 La Seur NE, Hawkins HF. 1963. An analysis of Hurricane Cleo (1958) based on data from research reconnaissance aircraft. *Mon. Weather Rev.*,
 175 **91**: 694-709.
 176 Malkus JS, Riehl H. 1960. On the dynamics and energy transformations in steady-state hurricanes. *Tellus*, **12**: 1-19.
 177 Marks FD, Black PG, Montgomery MT, Burpee RW. 2008. Structure of the eye and eyewall of Hurricane Hugo (1989). *Mon. Weather Rev.*, **136**:
 178 1237-1259.
 179 Montgomery MT, Smith RK. 2017. Recent developments in the fluid dynamics of tropical cyclones. *Annu. Rev. Fluid Mech.*, **49**: 1-33.
 180 Montgomery MT, Bell MM, Aberson SD, Black ML. 2006: Hurricane Isabel (2003): New insights into the physics off intense storms. Part I. Mean
 181 vortex structure and maximum intensity estimates. *Bull. Amer. Meteor. Soc.*, **87**: 1335-1347.

[‡]The quantity θ_e is calculated using Bolton's formula (Bolton, 1980, Equation (43)).

[§]The relative humidity is calculated relative to water saturation.

- 182 Munsell EB, Zhang F, Braun SA, Sippel JA, Didlake AC. 2018. The inner-core temperature structure of Hurricane Edouard (2014): Observations
183 and ensemble variability. *Mon. Weather Rev.*, **91**: 135-155.
- 184 Ooyama K. 1969. Numerical simulation of the life-cycle of tropical cyclones. *J. Atmos. Sci.*, **26**: 3-40.
- 185 Smith RK, Montgomery MT. 2013. How important is the isothermal expansion effect to elevating equivalent potential temperature in the hurricane
186 inner-core? *Q. J. R. Meteorol. Soc.*, **138**: 1-5.
- 187 Smith RK, Montgomery MT, Persing J. 2014. On steady-state tropical cyclones. *Q. J. R. Meteorol. Soc.*, **140**: 2638-2649.
- 188 Schmidt C, Smith RK. 2016. Tropical cyclone evolution in a minimal axisymmetric model revisited. *Q. J. R. Meteorol. Soc.*, **142**: 1505-1516.
- 189 Stewart, S. R., 2014: National Hurricane Center Tropical Cyclone Report: Hurricane Edouard (1119 September 2014). Tropical Cyclone Rep.
190 AL062014, National Hurricane Center, 19pp. Available online at http://www.nhc.noaa.gov/data/tcr/AL062014_Edouard.pdf.
- 191 Young K *et al.* 2016. Hurricane and Severe Storm Sentinel (HS3) 2014 Global Hawk Dropsonde Data Analysis Summary. [http://data.eol.](http://data.eol.ucar.edu/datafile/nph-get/348.004/readme.V3.HS3-2014.GHdropsonde.pdf)
192 [ucar.edu/datafile/nph-get/348.004/readme.V3.HS3-2014.GHdropsonde.pdf](http://data.eol.ucar.edu/datafile/nph-get/348.004/readme.V3.HS3-2014.GHdropsonde.pdf)
- 193 Wick, G., 2015: Hurricane and Severe Storm Sentinel (HS3) Global Hawk AVAPS Dropsonde System. NASA Global Hydrology Resource Center
194 DAAC, doi:<https://doi.org/10.5067/-HS3/AVAPS/DROPSONDE/DATA201>.
- 195 Zawislak J, Jiang H, Alvey GR, Zipser EJ, Rogers RF, Zhang JA, Stevenson SN. 2016. Observations of the structure and evolution of Hurricane
196 Edouard (2014) during intensity change. Part I: Relationship between the thermodynamic structure and precipitation. *Mon. Weather Rev.*, **144**: 3333-
197 3354.



Azimuthally-averaged structure of Hurricane Edouard (2014) just after peak intensity

Roger K. Smith^{a*}, Michael T. Montgomery^b and Scott Braun^c

^a Meteorological Institute, Ludwig Maximilians University of Munich, Munich, Germany

^b Dept. of Meteorology, Naval Postgraduate School, Monterey, CA, USA

^c Laboratory for Mesoscale Atmospheric Processes, NASA Goddard Space Flight Center, Greenbelt, Maryland, MD, USA

*Correspondence to: Prof. Roger K. Smith, Meteorological Institute, Ludwig-Maximilians University of Munich, Theresienstr. 37, 80333 Munich, Germany. E-mail: roger.smith@lmu.de

Analyses of dropsonde data just after the mature stage of Hurricane Edouard (2014) are presented. These data, which have unprecedentedly high spatial resolution, were obtained by the unmanned NASA Global Hawk during the Hurricane and Severe Storm Sentinel (HS3) field campaign. The analyses are related to theories of tropical cyclone structure and behaviour. In particular, the findings highlight the radial outflow above the boundary layer below about 8 km and between about 80 km and 220 km radius. This radial outflow would explain the observed spin down of the storm according to the classical mechanism. The findings highlight also a limitation of the assumed steadiness of the storm over the period of data collection.

Key Words: Tropical cyclone, hurricane, observed structure and behaviour

Received October 17, 2018; Revised ; Accepted

1. Introduction

In the past there have been few measurements of hurricane structure through the depth of the troposphere, the reason being that most aircraft reconnaissance flights have not been able to sample the upper troposphere. Some classic observational studies are those of La Seur and Hawkins (1963), Hawkins and Rubsam (1968) and Hawkins and Imbembo (1976) to whom *in situ* data from an instrumented high-flying jet aircraft were available. The situation changed recently through the deployment of the NASA* Global Hawk, an unmanned drone capable of releasing dropsondes in rapid succession from the lower stratosphere. During NASA's Hurricane and Severe Storm Sentinel (HS3; Braun *et al.* 2016) field campaign in 2014, comparatively high temporal and spatial resolution dropsonde observations were made over the Atlantic Ocean in Hurricane Edouard during four missions between 11 to 19 September 2014. A map showing the location of each dropsonde is contained in Figure 1 of Zawislak *et al.* (2016), while a description of the storm during its lifetime is given by Stewart (2014). Brief descriptions of the storm and the missions flown was given by Braun *et al.* (2016) and Munsell *et al.* (2018).

The structure of Edouard was particularly well sampled on 16–17 September while it was near peak intensity. On this mission, which lasted about 23 h, 87 dropsondes were deployed into the hurricane from a height of 18 km. The purpose of this paper is to present azimuthally averaged, radius-height cross sections of various quantities obtained from analyses of these unique data and to compare these analyses with theories of tropical cyclone behaviour.

2. Data

The 87 dropsondes were released into Edouard between 15:06 UTC 16 September and 08:28 UTC 17 September 2014 during which time the storm moved from about 32°N to 35°N (Stewart 2014, Table 1). The distribution of the dropsondes is shown in Abarca *et al.* (2016, Figure 2(a)). The sonde data were post-processed by NCAR using their Atmospheric Sounding Processing Environment (ASPEN) software (Young *et al.* 2016), see Wick *et al.* (2015). The original analyses of the dropsondes did not include a dry bias correction in the upper troposphere, but the present ones have used the correct humidity values. The analysis of these sondes is described briefly below.

*National Atmospheric and Space Administration

36 2.1. Computation of azimuthal averages

37 To calculate the azimuthal averages, the dropsonde data were first interpolated to 181 pressure levels with a spacing of 5 mb. The storm
38 centre positions over the time period of the flight were used to determine the location of each dropsonde relative to the evolving centre
39 position. The National Hurricane Center best track data were used also to estimate the mean storm motion over the flight period. The
40 positions of the dropsonde data were shifted to a reference time of 00 UTC 17 September using the storm motion and the time difference
41 between the sonde time and this reference time. Here, the sonde time is the time of the actual measurement at a particular level. Using
42 these adjusted positions relative to the centre, radial and tangential velocities were calculated with the storm motion removed to obtain
43 storm-relative flow. This analysis was done for all dropsondes during the flight. Bins were then created for averaging after all derived
44 fields such as radial and tangential velocity were calculated.

45 The midpoints of the bins were at radial locations 10, 35, 70, 110, 170, 245, 320, 400, 480 and 560 km from the centre[†]. The number
46 of soundings were distributed within each bin as follows: 0-20 km radius (10 sondes), 20-40 km (9), 40-60 km (7), 60-90 km (10),
47 90-120 km (8), 120-200 km (3), 200-280 km (14), 280-360 km (9), 360-440 km (8), 440-520 km (8), 520-600 km (7). No additional
48 smoothing was applied to the individual dropsonde data. If, when computing the azimuthal mean, some values were missing from
49 individual soundings, they were simply not included in the calculation of the mean. For the height-radius coordinate used in the plots
50 to be shown, there were no missing azimuthal mean values.

51 2.2. Steady-state composite data

52 Although the storm was at peak intensity near the start of measurements, the intensity decreased by about 10 m s^{-1} during the period
53 of measurements (see Abarca *et al.* 2016, Figure 1 and accompanying discussion of the various factors in this decay). Attempts were
54 made to subdivide the data into two separate subsets, one in the first half of the flight and another in the second half. The number of
55 soundings were distributed as follows over the course of the first half of the flight, and the second half of the flight: radius 0-20 km
56 (first half 6, second half 4), 20-40 km (4, 5), 40-60 km (5, 3), 60-90 km (4, 7), 90-120 km (4, 4), 120-200 km (2, 1), 200-280 km (6,
57 8), 280-360 km (3, 6), 360-440 km (3, 5), 440-520 km (3, 5), 520-600 km (2, 5). Clearly, breaking up the soundings into two separate
58 halves of the flight reduces the number of samples in each radial bin, although not necessarily by half since a good part of the first half
59 of the flight was sampling storm outflow beyond 600 km radius. The biggest problem occurs in the 120-200 km radius bin, where the
60 second half of the flight has only one sounding, and much of that data is missing, so contours cannot be drawn there. For these reasons,
61 and because there was qualitative similarity between the derived structures from the two data sets in regions where there was data, we
62 have based the analysis below on a composite for the whole period. Thus, all the storm-relative dropsonde data from the whole flight
63 occurring within a particular bin were averaged. This procedure is tantamount to assuming the storm to be in a steady state for the
64 duration of the flight. Some limitations of the steady state assumption will emerge later.

65 3. Storm structure

66 Figure 1 shows radius-height cross sections obtained from the dropsonde data as described in subsection 2.1 above. The data are slightly
67 smoothed using a centred 1-4-1 box filter applied 10 times.

68 3.1. Tangential wind and warm core structure

69 The storm-relative composite tangential wind component (v , Figure 1a) and temperature perturbation (dT , panel (b)) show the classical
70 structure of a warm-cored vortex with the maximum wind in the lower troposphere and the wind decreasing with height, becoming
71 anticyclonic in the upper troposphere. The decrease in the tangential velocity component with height corresponds through balance
72 considerations with the warm-core structure (see Figure 1b)

73 There is evidence of a secondary tangential wind maximum at a radius of about 100 km, the inner maximum being near 50 km
74 radius. The formation of this secondary wind maximum was the focus of a separate study (Abarca *et al.* 2016, see below for more).
75 The upper-level anticyclone begins at a radius of about 80 km, while the strength of the anticyclone increases with radius and the
76 anticyclonic circulation deepens with increasing radius. The maximum anticyclonic flow is found at an altitude between 14 and 15 km.

77 Figure 1(a) shows also the absolute angular momentum (or M -) surfaces corresponding with the tangential wind component. These
78 are calculated using the formula $M = rv + \frac{1}{2}fr^2$, where r is the radius and f is the Coriolis parameter at the mean latitude of Edouard
79 (33 N) during the period of dropsonde measurements. Consistent with theoretical expectations, the M -surfaces flare outwards with
80 height, with M mostly increasing with radius and decreasing with height. There is an elevated local maximum of M located at a height
81 of about 5.5 km and a radius of about 410 km and two additional maxima at larger radii. These maxima are accompanied by a negative
82 radial gradient of M at radii beyond them, implying that the flow is inertially unstable. Since the dropsonde data at these radii are rather
83 sparse (see Abarca *et al.* 2016, Figure 2(b)) and the period of collection spans an interval of more than 16 h, we do not attribute much
84 significance to the implied regions of instability at these radii.

85 There is a marked positive temperature anomaly inside a radius varying between 100-150 km, depending on height (Figure 1(b)).
86 (For the calculation of temperature perturbation, the “environmental temperature” was determined by averaging all dropsonde data at
87 radii > 200 km. Specifically, there were 46 soundings used in calculation of the “environmental” mean temperature for the temperature
88 perturbation plot.) The temperature anomaly has a maximum of nearly 10°C at an altitude of about 8 km close to the axis of rotation.
89 There is a weak cold temperature anomaly at low levels beyond about 50 km radius. The negative temperature anomalies beyond about
90 400 km are due to the way the ambient temperature has been defined (see section 2.1). Since the reference temperature is based on an
91 average of all soundings beyond a radius of 200 km and if the temperature in this region decreases outwards, negative anomalies would
92 be expected at large radii. The low-level negative anomaly between 100 and 300 km radius is presumably a result of the evaporation of
93 falling raindrops.

[†]The data set is the same as that used by Abarca *et al.* (2016). However, the subdivision into bins is somewhat different. Even so, the tangential wind field in Abarca *et al.* (Figure 3(a)) is very similar to that shown in Figure 1(a). The pressure field is rather smooth and should be similar between the two analyses. Indeed, Abarca *et al.* did note that “the data were robust to different bin-length choices”.

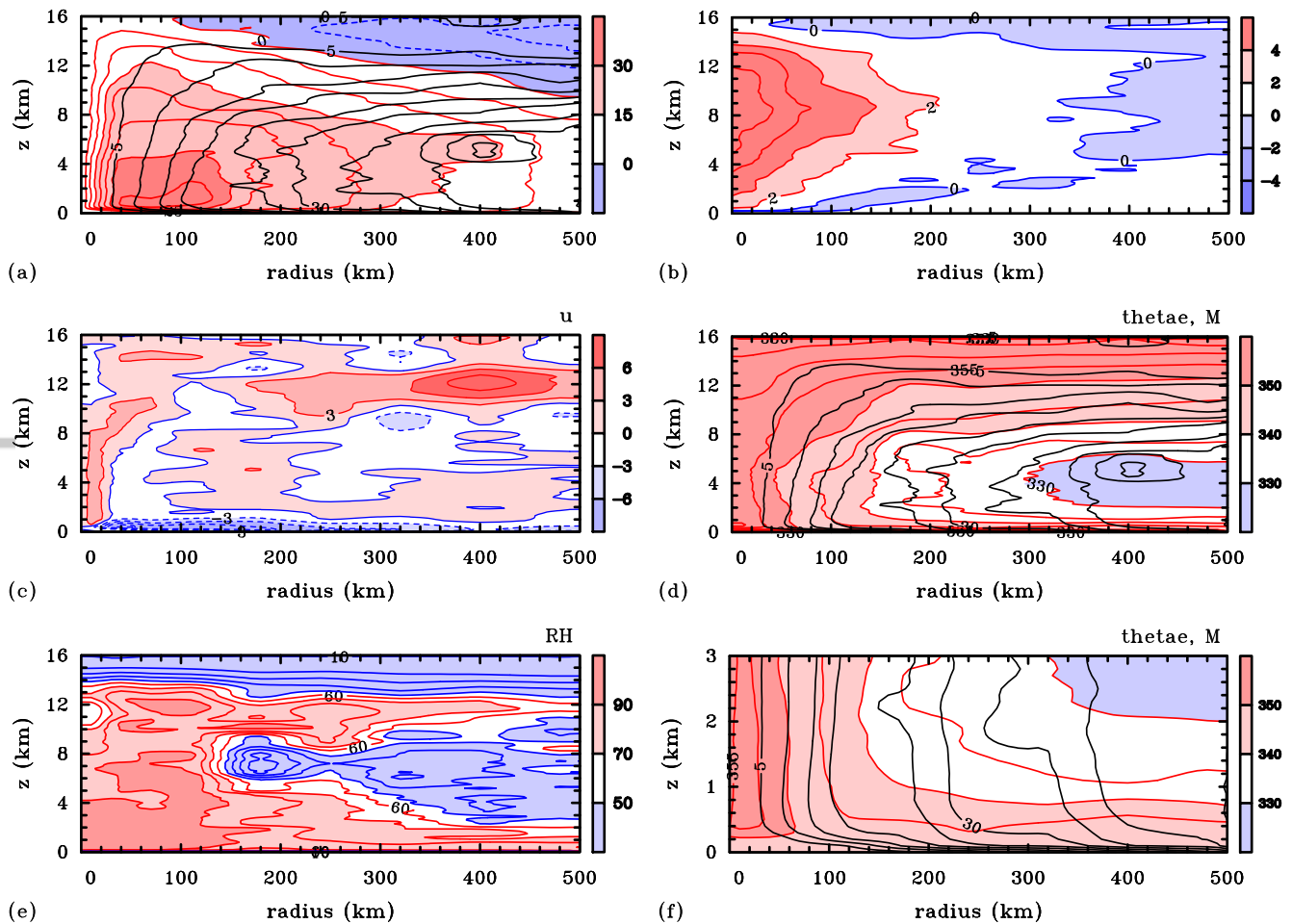


Figure 1. Radius-height cross sections of selected fields derived from the dropsonde data: (a) tangential velocity component, contour interval 5 m s^{-1} , shading indicated on the side bar in m s^{-1} , and absolute angular momentum, black lines, contour interval $5 \times 10^5 \text{ m}^2 \text{ s}^{-1}$; (b) temperature perturbation, contour interval 2 K (positive values), 1 K (negative values), shading indicated on the side bar in K; (c) radial velocity component, contour interval 3 m s^{-1} , shading indicated on the side bar in m s^{-1} ; (d) equivalent potential temperature, contour interval 10 K, shading indicated on the side bar in K, and absolute angular momentum, black lines, contours as in (a); (e) relative humidity, contour interval 10%, shading indicated on the side bar in %; (f) a zoomed in version of panel (d) at heights below 3 km.

94 3.2. Radial velocity component

95 The storm-relative composite radial flow (u , Figure 1c) shows two features of the classical tropical cyclone structure with a layer of
 96 strong inflow below about 1 km extending to large radii as well as a layer of strong outflow in the upper troposphere between about 9
 97 and 14 km depending on radius. The maximum low-level inflow is about 15 m s^{-1} . The layer of upper tropospheric outflow is a few
 98 km deep with a maximum of nearly 12 m s^{-1} at about 12 km altitude and 400 km radius.

99 Perhaps surprisingly, the layers of anticyclonic flow and outflow in the upper troposphere have only a small overlap and mainly at
 100 large radii. In particular, the level of maximum outflow does not coincide with that of the maximum anticyclonic flow, which is typically
 101 2 km higher. A plausible explanation is that during the earlier part of the period of investigation, the outflow was higher than during
 102 the later part. This possibility is supported by the fact that the region of strong outflow begins beyond 100 km radius near where the
 103 secondary wind maximum and secondary eyewall have formed (cf. Abarca *et al.* 2016). In the region inside a radius of 100 km, there
 104 is a localized region of outflow with a maximum near 14 km height, presumably remnants of the previous outflow at a higher level.
 105 **The foregoing difficulty in reconciling the radial and tangential structure of the storm highlights a potential limitation of assuming that
 106 the storm is in a quasi-steady state for the purpose of the analysis.**

107 Another interesting feature of the radial flow is the broad region of outflow inside a radius of about 220 km in the lower half of the
 108 troposphere above the shallow surface-based boundary layer inflow. This outflow has two local maxima, the inner one associated in
 109 part with the inner eyewall and the outer one with the secondary eyewall and secondary wind maximum as documented in Abarca *et al.*
 110 (2016). This pattern of outflow would suggest that the flow in these regions is spinning down by the outward radial advection of
 111 the M -surfaces. However, this spin down effect would be countered by the vertical advection of air with high values of M from the
 112 boundary layer. It was shown by Abarca *et al.* (2016, see their Figure 4b), that the boundary layer flow was supergradient below both
 113 the primary and secondary eyewalls on the day prior to the present observations. The fact that the storm had just begun to weaken (see
 114 section 2.1) would indicate that the spin down tendency due to the outward radial advection of the M -surfaces would be dominant,
 115 at least for the primary eyewall. The role of the vertical advection of supergradient values of M from the boundary layer to spin up
 116 the primary eyewall was highlighted by the study of Schmidt and Smith (2016) using a minimal three-layer numerical model and was
 117 discussed in a more general context by Montgomery and Smith (2017: section 3.9).

118 **Beyond the 220 km radius in Figure 1c, there are alternate layers of inflow and outflow with outflow being the dominant feature
 119 between about 1.5 km and up to 5 km in height.**

120 Other interesting features of the radial flow are the layers of inflow in the upper troposphere, above and below the outflow layer.
 121 Such features are often seen in numerical model simulations, but to our knowledge are not well understood.

122 3.3. Pseudo-equivalent potential temperature

123 The distribution of pseudo-equivalent potential temperature[‡], θ_e , (Figure 1d and 1f) shows the classical structure also. (Figure 1f is a
 124 zoomed in plot of Figure 1d in the lowest 3 km.) Principal features are: the mid-tropospheric minimum beyond a radius of about 100
 125 km, increasing in prominence with radius; the tendency for the isopleths of θ_e to become close to vertical in the lower troposphere
 126 inside a radius of 100 km; and the tendency for the isopleths of θ_e to slope outwards and become close to horizontal in the upper
 127 tropospheric outflow layer. There is an approximate congruence between the θ_e - and M -surfaces in the inner core region and in the
 128 upper troposphere (the M -surfaces are shown also in Figure 1d and 1f). This approximate congruence in the inner-core region ($r < 200$
 129 km) forms the cornerstone of the steady-state axisymmetric hurricane model by Emanuel (1986).

130 Throughout much of the troposphere, θ_e has a negative radial gradient. This is, in part, a reflection of the structure in the boundary
 131 layer. In this layer (below 1 km) the negative radial gradient of θ_e is apparent only inside a radius of about 100 km and is a result
 132 of the presumed increase in surface moisture flux with decreasing radius (Malkus and Riehl 1960, Ooyama 1969). Such a localized
 133 gradient was documented in the classical observational analysis of Hawkins and Imbembo (1976) and has been confirmed by more
 134 recent work (Montgomery *et al.* 2006, Marks *et al.* 2008, Bell and Montgomery 2008, Smith and Montgomery 2013). Maximum values
 135 of θ_e exceed 355 K in the low to mid troposphere near and inside the eyewall region. The surface value is approximately constant at
 136 350 K outside of 100 km radius. The minimum value in the mid to low troposphere falls to values less than 320 K beyond about 300
 137 km radius (the region highlighted in blue in Figure 1d).

138 3.4. Relative humidity

139 Values of relative humidity[§], (RH , panel(d)), exceed 90% inside a radius of 200 km and below about 7 km altitude. At larger radii,
 140 values are high ($> 80\%$) in a shallow near-surface layer, but decrease markedly with height with values of less than 50% through much
 141 of the troposphere, especially beyond about 300 km in radius. These low values are an indication of drying in the subsiding branch of
 142 the secondary circulation. This plot does indicate a couple of features of interest. First, the RH starts to drop off beyond the secondary
 143 wind maximum, perhaps suggesting that this wind maximum either forms near the boundary with dry air or acts as a potential barrier
 144 to dry air. Second, very dry air is being drawn inwards just below the outflow layer.

145 4. Conclusions

146 In this paper we have used a dropsonde data set with unprecedentedly high spatial coverage from the NASA HS3 experiment to analyze
 147 the azimuthally-averaged structure of Hurricane Edouard (2014) just after its peak intensity. The dropsondes were deployed from above
 148 the tropopause and enable a sampling of the full troposphere. The analyses of these unique observations confirm many known structural
 149 features of a mature tropical cyclone, e.g. tangential wind structure, radial wind structure, warm core structure and equivalent potential
 150 temperature structure. In particular, they show radial outflow above the boundary layer in the lower half of the troposphere and inside
 151 about 220 km radius, which would explain the observed spin down of the storm as absolute angular momentum surfaces are advected
 152 outwards. Nevertheless, even with such an unprecedentedly high density of dropsondes to estimate the azimuthally-averaged structure,
 153 there remains an issue in reconciling the radial and tangential structure of the hurricane. This issue appears to arise from the analysis
 154 assumption of a quasi-steady state during the period of observations, an assumption that stands out as an important limitation of any
 155 analysis of dropsonde data over such an extended period of observations as the one in this case.

156 5. Acknowledgements

157 We thank Jun Zhang and two anonymous reviewers for their perceptive and constructive comments on the original manuscript. RKS
 158 acknowledges financial support for tropical cyclone research from the Office of Naval Research Global under Grant No. N62909-15-
 159 1-N021. MTM acknowledges the support of NSF grant AGS-1313948, NOAA HFIP grant N0017315WR00048, NASA (HS3) grant
 160 NNG11PK021, ONR grant N0001417WX00336, and the U. S. Naval Postgraduate School.

161 6. References

- 162 Abarca SF, Montgomery MT, Braun SA, Dunion J. 2016. On the secondary eyewall formation of Hurricane Edouard (2014). *Mon. Weather Rev.*, **144**:
 163 3321-3331.
 164 Bell MM, Montgomery MT. 2008. Observed structure, evolution, and potential intensity of Category 5 Hurricane Isabel (2003) from 12 to 14
 165 September. *Mon. Weather Rev.*, **65**: 2025-2046.
 166 Bolton D. 1980. The computation of equivalent potential temperature. *Mon. Weather Rev.*, **108**: 1046-053.
 167 Braun SA and Coauthors, 2013: NASAs Genesis and Rapid Intensification Processes (GRIP) field experiment. *Bull. Amer. Meteor. Soc.*, **94**: 345-363.
 168 Braun, SA, Newman PA, Heymsfield GM. 2016. NASAs Hurricane and Severe Storm Sentinel (HS3) investigation. *Bull. Amer. Meteor. Soc.*, **97**:
 169 2085-2102.
 170 Emanuel KA, 1986. An air-sea interaction theory for tropical cyclones. Part I: steady state maintenance. *J. Atmos. Sci.*, **43**: 585-604.
 171 Hawkins HF, Rubsam DT. 1968: Hurricane Hilda, 1964. II: Structure and budgets of the hurricane on October 1, 1964. *Mon. Weather Rev.*, **96**:
 172 617-636.
 173 Hawkins HF, Imbembo SM. 1976. The structure of a small, intense Hurricane Inez 1966. *Mon. Weather Rev.*, **104**: 418-442.
 174 La Seur NE, Hawkins HF. 1963. An analysis of Hurricane Cleo (1958) based on data from research reconnaissance aircraft. *Mon. Weather Rev.*,
 175 **91**: 694-709.
 176 Malkus JS, Riehl H. 1960. On the dynamics and energy transformations in steady-state hurricanes. *Tellus*, **12**: 1-19.
 177 Marks FD, Black PG, Montgomery MT, Burpee RW. 2008. Structure of the eye and eyewall of Hurricane Hugo (1989). *Mon. Weather Rev.*, **136**:
 178 1237-1259.
 179 Montgomery MT, Smith RK. 2017. Recent developments in the fluid dynamics of tropical cyclones. *Annu. Rev. Fluid Mech.*, **49**: 1-33.
 180 Montgomery MT, Bell MM, Aberson SD, Black ML. 2006: Hurricane Isabel (2003): New insights into the physics off intense storms. Part I. Mean
 181 vortex structure and maximum intensity estimates. *Bull. Amer. Meteor. Soc.*, **87**: 1335-1347.

[‡]The quantity θ_e is calculated using Bolton's formula (Bolton, 1980, Equation (43)).

[§]The relative humidity is calculated relative to water saturation.

- 182 Munsell EB, Zhang F, Braun SA, Sippel JA, Didlake AC. 2018. The inner-core temperature structure of Hurricane Edouard (2014): Observations
183 and ensemble variability. *Mon. Weather Rev.*, **91**: 135-155.
- 184 Ooyama K. 1969. Numerical simulation of the life-cycle of tropical cyclones. *J. Atmos. Sci.*, **26**: 3-40.
- 185 Smith RK, Montgomery MT. 2013. How important is the isothermal expansion effect to elevating equivalent potential temperature in the hurricane
186 inner-core? *Q. J. R. Meteorol. Soc.*, **138**: 1-5.
- 187 Smith RK, Montgomery MT, Persing J. 2014. On steady-state tropical cyclones. *Q. J. R. Meteorol. Soc.*, **140**: 2638-2649.
- 188 Schmidt C, Smith RK. 2016. Tropical cyclone evolution in a minimal axisymmetric model revisited. *Q. J. R. Meteorol. Soc.*, **142**: 1505-1516.
- 189 Stewart, S. R., 2014: National Hurricane Center Tropical Cyclone Report: Hurricane Edouard (1119 September 2014). Tropical Cyclone Rep.
190 AL062014, National Hurricane Center, 19pp. Available online at http://www.nhc.noaa.gov/data/tcr/AL062014_Edouard.pdf.
- 191 Young K *et al.* 2016. Hurricane and Severe Storm Sentinel (HS3) 2014 Global Hawk Dropsonde Data Analysis Summary. [http://data.eol.](http://data.eol.ucar.edu/datafile/nph-get/348.004/readme.V3.HS3-2014.GHdropsonde.pdf)
192 [ucar.edu/datafile/nph-get/348.004/readme.V3.HS3-2014.GHdropsonde.pdf](http://data.eol.ucar.edu/datafile/nph-get/348.004/readme.V3.HS3-2014.GHdropsonde.pdf)
- 193 Wick, G., 2015: Hurricane and Severe Storm Sentinel (HS3) Global Hawk AVAPS Dropsonde System. NASA Global Hydrology Resource Center
194 DAAC, doi:<https://doi.org/10.5067/-HS3/AVAPS/DROPSONDE/DATA201>.
- 195 Zawislak J, Jiang H, Alvey GR, Zipser EJ, Rogers RF, Zhang JA, Stevenson SN. 2016. Observations of the structure and evolution of Hurricane
196 Edouard (2014) during intensity change. Part I: Relationship between the thermodynamic structure and precipitation. *Mon. Weather Rev.*, **144**: 3333-
197 3354.

Author Manuscript



Azimuthally-averaged structure of Hurricane Edouard (2014) just after peak intensity

Roger K. Smith^{a*}, Michael T. Montgomery^b and Scott Braun^c

^a *Meteorological Institute, Ludwig Maximilians University of Munich, Munich, Germany*

^b *Dept. of Meteorology, Naval Postgraduate School, Monterey, CA, USA*

^c *Laboratory for Mesoscale Atmospheric Processes, NASA Goddard Space Flight Center, Greenbelt, Maryland, MD, USA*

*Correspondence to: Prof. Roger K. Smith, Meteorological Institute, Ludwig-Maximilians University of Munich, Theresienstr. 37, 80333 Munich, Germany. E-mail: roger.smith@lmu.de

Analyses of dropsonde data collected in Hurricane Edouard (2014) just after its mature stage are presented. These data, have unprecedentedly high spatial resolution, based on 87 dropsondes released by the unmanned NASA Global Hawk from an altitude of 18 km during the Hurricane and Severe Storm Sentinel (HS3) field campaign. Attempts are made to relate the analyses of the data to theories of tropical cyclone structure and behaviour. The tangential wind and thermal fields show the classical structure of a warm core vortex, in this case with a secondary eyewall feature. The equivalent potential temperature (θ_e) field shows also the expected structure with a mid-tropospheric minimum at outer radii and contours of θ_e flaring upwards and outwards at inner radii and, with some imagination, roughly congruent to the surfaces of absolute angular momentum. However, details of the analysed radial velocity field are somewhat sensitive to the way in which the sonde data are partitioned to produce an azimuthal average. This sensitivity is compounded by an apparent limitation of the assumed steadiness of the storm over the period of data collection.

Key Words: Tropical cyclone, hurricane, observed structure and behaviour

Received November 9, 2018; Revised ; Accepted

1. Introduction

In the past there have been few measurements of hurricane structure through the depth of the troposphere, the reason being that most aircraft reconnaissance flights have not been able to sample the upper troposphere. Some classic observational studies are those of La Seur and Hawkins (1963), Hawkins and Rubsam (1968) and Hawkins and Imbembo (1976) to whom *in situ* data from an instrumented high-flying jet aircraft were available. The situation changed recently through the deployment of the NASA* Global Hawk, an unmanned drone capable of releasing dropsondes in rapid succession from the lower stratosphere. During NASA's Hurricane and Severe Storm Sentinel (HS3; Braun *et al.* 2016) field campaign in 2014, comparatively high temporal and spatial resolution dropsonde observations were made over the Atlantic Ocean in Hurricane Edouard during four missions between 11 to 19 September 2014. A map showing the location of each dropsonde is contained in Figure 1 of Zawislak *et al.* (2016), while a description of the storm during its lifetime is given by Stewart (2014). Brief descriptions of the storm and the missions flown was given by Braun *et al.* (2016) and Munsell *et al.* (2018).

The structure of Edouard was particularly well sampled on 16-17 September while it was near peak intensity. On this mission, which lasted about 23 h, 87 dropsondes were deployed into the hurricane from a height of 18 km. The purpose of this paper is to present azimuthally averaged, radius-height cross sections of various quantities obtained from analyses of these unique data and to compare these analyses with theories of tropical cyclone behaviour.

2. Data

The 87 dropsondes were released into Edouard between 15:06 UTC 16 September and 08:28 UTC 17 September 2014 during which time the storm moved from about 32 N to 35 N (Stewart 2014, Table 1). The distribution of the dropsondes is shown in Abarca *et al.*

*National Atmospheric and Space Administration

(2016, Figure 2(a)). The sonde data were post-processed by NCAR (see Wick *et al.* 2015) using their Atmospheric Sounding Processing Environment (ASPEN) software (Young *et al.* 2016). The original analyses of the dropsondes did not include a dry bias correction in the upper troposphere, but the present ones have used the correct humidity values. The analysis of these sondes is described briefly below.

2.1. Computation of azimuthal averages

To calculate the azimuthal averages, the dropsonde data were first interpolated to 181 pressure levels with a spacing of 5 mb. The storm centre positions over the time period of the flight were used to determine the location of each dropsonde relative to the evolving centre position. The National Hurricane Center best track data were used also to estimate the mean storm motion over the flight period. The positions of the dropsonde data were shifted to a reference time of 00 UTC 17 September using the storm motion and the time difference between the sonde time and this reference time. Here, the sonde time is the time of the actual measurement at a particular level. Using these adjusted positions relative to the centre, radial and tangential velocities were calculated with the storm motion removed to obtain storm-relative flow. This analysis was done for all dropsondes during the flight. Bins were then created for averaging after all derived fields such as radial and tangential velocity were calculated.

The midpoints of the bins were at radial locations 10, 30, 50, 70, 100, 150, 210, 270, 330, 400, 480, and 560 km from the centre[†]. The number of soundings were distributed within each bin as follows: 0-20 km radius (11 sondes), 20-40 km (9), 40-60 km (6), 60-80 km (7), 80-120 km (10), 120-180 km (0), 180-240 km (9), 240-300 km (8), 300-360 km (8), 360-440 km (4), 440-520 km (8), 520-600 km (7). No additional smoothing was applied to the individual dropsonde data. If, when computing the azimuthal mean, some values were missing from individual soundings, they were simply not included in the calculation of the mean. Because there were no dropsonde data at radii between 120 km and 200 km and therefore in the radial bin 120-180 km, the azimuthal values for 150 km radius were determined by linear interpolation between the bin midpoints at 100 km and 210 km.

2.2. Steady-state composite data

Although the storm was at peak intensity near the start of measurements, the intensity decreased by about 10 m s^{-1} during the period of measurements (see Abarca *et al.* 2016, Figure 1 and accompanying discussion of the various factors in this decay). Because of the relatively long period of data collection, attempts were made to subdivide the data into two separate subsets, one in the first half of the flight and another in the second half. In this subdivision the number of soundings were distributed as follows over the course of the first half of the flight, and the second half of the flight: radius 0-20 km (first half 6, second half 5), 20-40 km (4, 5), 40-60 km (3, 3), 60-80 km (3, 4), 80-120 km (5, 5), 120-180 km (0, 0), 180-240 km (4, 5), 240-300 km (4, 4), 300-360 km (3, 5), 360-440 km (1, 3), 440-520 km (3, 5), 520-600 km (2, 5). Clearly, breaking up the soundings into two separate halves of the flight reduces the number of samples in each radial bin, although not necessarily by half since a good part of the first half of the flight was sampling storm outflow beyond 600 km radius. As mentioned earlier, the biggest problem occurs between 120-180 km, where there are no soundings for either time. For these reasons, and because there was qualitative similarity between the derived structures from the two data sets in regions where there was data, we have based the analysis below on a composite for the whole period. Thus, all the storm-relative dropsonde data from the whole flight occurring within a particular bin were averaged. This procedure is tantamount to assuming the storm to be in a quasi-steady state for the duration of the flight. Some limitations of the quasi-steady state assumption will emerge later.

3. Storm structure

Figure 1 shows radius-height cross sections obtained from the dropsonde data as described in subsection 2.1 above. The wind data are smoothed using a centred 1-4-1 box filter applied 10 times.

3.1. Tangential wind and warm core structure

The storm-relative composite tangential wind component (v , Figure 1a) and temperature perturbation (dT , panel (b)) show the classical structure of a warm-cored vortex with the maximum wind in the lower troposphere and the wind decreasing with height, becoming anticyclonic in the upper troposphere. The decrease in the tangential velocity component with height corresponds through balance considerations with the warm-core structure (see Figure 1b).

There is evidence of a weak inner tangential wind maximum near 40 km and an outer maximum at a radius of about 100 km. The formation of the outer wind maximum was the focus of a separate study by Abarca *et al.* (2016). The upper-level anticyclone begins at a radius of about 80 km, while the strength of the anticyclone increases with radius and the anticyclonic circulation deepens with increasing radius. The maximum anticyclonic flow is found at an altitude between 14 and 15 km at 500 km radius and is clearly increasing beyond this radius.

Figure 1(a) shows also the absolute angular momentum (or M -) surfaces corresponding with the tangential wind component. These are calculated using the formula $M = rv + \frac{1}{2}fr^2$, where r is the radius and f is the Coriolis parameter at the mean latitude of Edouard (33°N) during the period of dropsonde measurements. Consistent with theoretical expectations, the M -surfaces flare outwards with height, with M mostly increasing with radius and decreasing with height. There is a local maximum of M , located at a height of about 6 km and a radius of just over 400 km. This maximum is accompanied by a negative radial gradient of M at radii beyond it, implying that, according to linear theory, the flow would be centrifugally unstable locally (Rayleigh, 1916). Since the dropsonde data at these radii are rather sparse (see Abarca *et al.* 2016, Figure 3(b)) and the period of collection spans an interval of more than 16 h, we do not attribute much significance to the implied regions of instability at these radii.

[†]The data set is the same as that used by Abarca *et al.* (2016). However, the subdivision into bins is somewhat different. Even so, the tangential wind field in Abarca *et al.* (Figure 3(a)) is very similar to that shown in Figure 1(a). The pressure field is rather smooth and should be similar between the two analyses. Indeed, Abarca *et al.* did note that “the data were robust to different bin-length choices”.

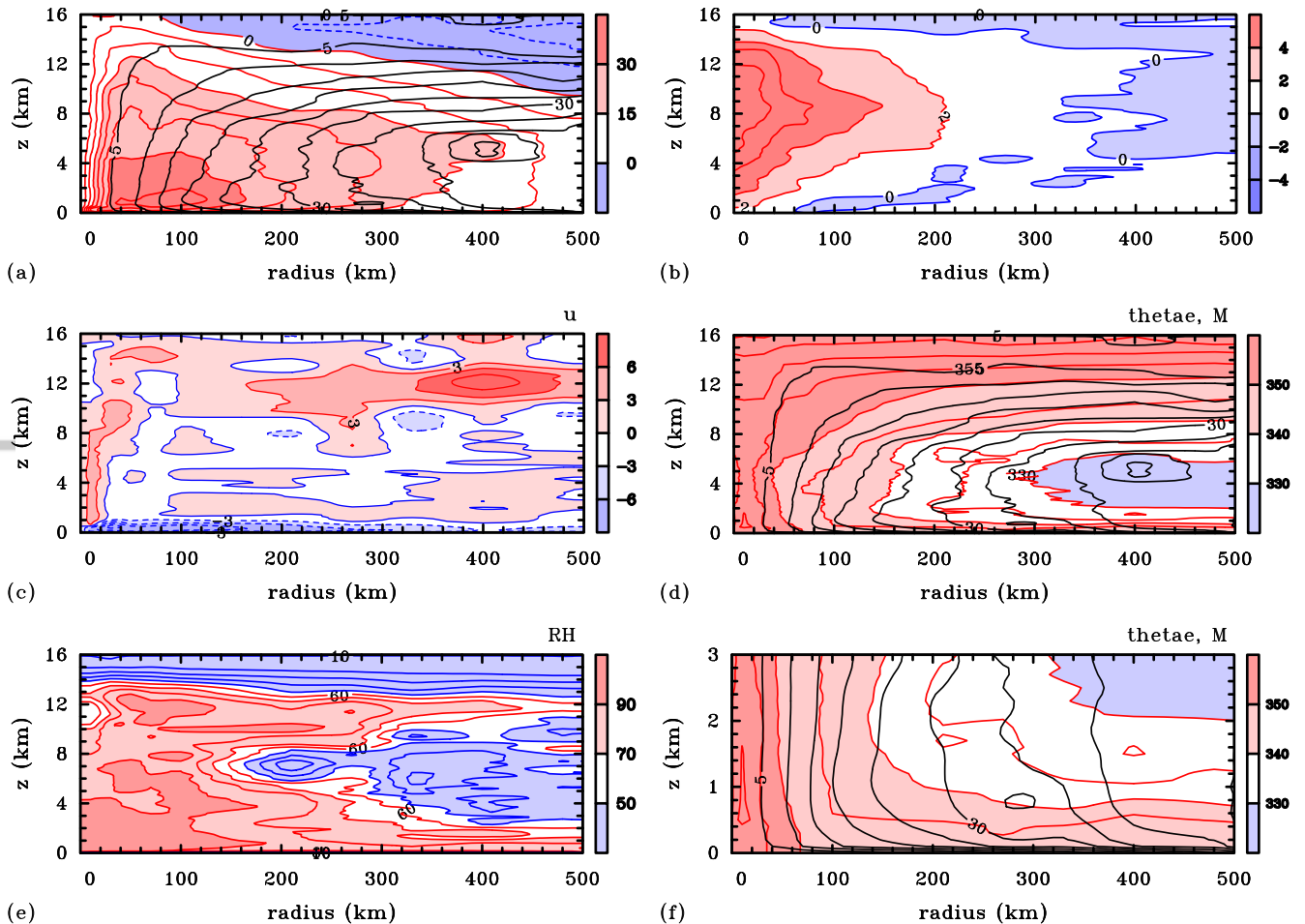


Figure 1. Radius-height cross sections of selected fields derived from the dropsonde data: (a) tangential velocity component, contour interval 5 m s^{-1} , shading indicated on the side bar in m s^{-1} , and absolute angular momentum, black lines, contour interval $5 \times 10^5 \text{ m}^2 \text{ s}^{-1}$; (b) temperature perturbation, contour interval 2 K (positive values), 1 K (negative values), shading indicated on the side bar in K; (c) radial velocity component, contour interval 3 m s^{-1} , shading indicated on the side bar in m s^{-1} ; (d) equivalent potential temperature, contour interval 10 K, shading indicated on the side bar in K, and absolute angular momentum, black lines, contours as in (a); (e) relative humidity, contour interval 10%, shading indicated on the side bar in %; (f) a zoomed in version of panel (d) at heights below 3 km.

There is a marked ($> 2^\circ\text{C}$) positive temperature anomaly inside a radius of about 200 km (Figure 1(b)). This anomaly has a maximum of nearly 10°C on the axis of rotation at an altitude of about 8 km. (For the calculation of temperature perturbation, the “environmental temperature” was determined by averaging all dropsonde data at radii > 200 km. Specifically, there were 46 soundings used in calculation of the “environmental” mean temperature for the temperature perturbation plot.) There is a weak cold temperature anomaly at low levels beyond about 60 km radius. The negative temperature anomalies beyond about 400 km radius and those above 13 km are due to the way the ambient temperature has been defined and are presumably not significant. Since the reference temperature is based on an average of all soundings beyond a radius of 200 km and if the temperature in this region decreases outwards, negative anomalies would be expected at large radii. The low-level negative anomaly between 60 and 240 km radius is plausibly a result of the evaporation of falling raindrops.

3.2. Radial velocity component

The storm-relative composite radial flow (u , Figure 1c) shows two features of the classical tropical cyclone structure with a layer of strong inflow below about 1 km extending to large radii as well as a layer of strong outflow in the upper troposphere between about 9 and 14 km depending on radius. The maximum low-level inflow is about 15 m s^{-1} . The layer of upper tropospheric outflow is a few km deep with a maximum of nearly 12 m s^{-1} at about 12 km altitude and 400 km radius.

Perhaps surprisingly, the level of maximum outflow in the upper troposphere does not coincide with that of the maximum anticyclonic flow, which is typically 2 km higher. A plausible explanation for this finding is that during the earlier period of measurement, the outflow was higher than during the later part. This possibility is supported by the fact that there are two layers of outflow, one centred around 14 km height, emanating from the inner eyewall and another, centred around 12 km height, emanating from the outer eyewall (see Abarca *et al.* 2016 for further details of the double eyewall structure). The upper layer has its maximum well within a radius of 100 km, whereas the lower maximum, which is much stronger, occurs at a radius of 400 km. The foregoing issue in reconciling the radial and tangential wind structure in the upper troposphere highlights a potential limitation of assuming that the storm is in a quasi-steady state for the purpose of the analysis.

In the lower troposphere there are significant regions of outflow above the shallow surface-based boundary layer inflow. This outflow has a local maximum in the inner eyewall (near 20 km radius) and has a layered structure beyond a radius of about 90 km starting near outer eyewall. This pattern of outflow would suggest that the flow in these regions is spinning down by the outward radial advection of the M -surfaces. However, this spin down effect would be countered by the vertical advection of air with high values of M from the boundary layer, at least in the inner core region. In this context, it was shown by Abarca *et al.* (2016, see their Figure 4b), that the

boundary layer flow was supergradient below both the primary and secondary eyewalls on the day prior to the present observations. The fact that the storm had just begun to weaken (see section 2.1) would indicate that the spin down tendency due to the outward radial advection of the M -surfaces would be dominant, at least for the inner eyewall. The role of the vertical advection of supergradient values of M from the boundary layer to spin up the inner eyewall was highlighted by the study of Schmidt and Smith (2016) using a minimal three-layer numerical model and was discussed in a more general context by Montgomery and Smith (2017: section 3.9).

Beyond about 300 km radius in Figure 1c, where the boundary layer flow is typically subgradient, there is mostly outflow in the lower troposphere above the boundary layer. At such radii, this outflow would carry the M surfaces outwards leading to a spin-down of the tangential winds and therefore a contracting in the storm size (see Kilroy *et al.* 2016 for a discussion of the factors influencing storm size).

Other interesting features of the radial flow are the layers of inflow in the upper troposphere, above and below the two outflow layers. Such features are often seen in numerical model simulations (e.g. Rotunno and Emanuel 1987, Figure 5c; Persing *et al.* 2013, Figures 10a, 11a, 15a; Montgomery *et al.* 2018, Figures 7b, 8b), but to our knowledge are not well understood.

It should be pointed out that while the broad features of the analyzed radial flow field are robust (e.g. the strong inflow in the boundary layer, the upper-level outflow and the outflow in the inner and outer eyewalls), the details of this field are somewhat sensitive to the way in which the sonde data are binned to produce an azimuthal average (not shown). This sensitivity is compounded by an apparent limitation of the assumed steadiness of the storm over the period of data collection discussed above.

3.3. Pseudo-equivalent potential temperature

The distribution of pseudo-equivalent potential temperature[‡], θ_e , (Figure 1d and 1f) shows the classical structure also. (Figure 1f is a zoomed in plot of Figure 1d in the lowest 3 km.) Principal features are: the mid-tropospheric minimum beyond a radius of about 100 km, increasing in prominence with radius; the tendency for the isopleths of θ_e to become close to vertical in the lower troposphere inside a radius of 100 km; and the tendency for the isopleths of θ_e to slope outwards and become close to horizontal in the upper tropospheric outflow layer. With a little imagination, there is an approximate congruence between the θ_e - and M -surfaces in the inner core region and in the upper troposphere, at least out to 250 km radius (the M -surfaces are shown also in Figure 1d and 1f). This approximate congruence forms the cornerstone of the steady-state axisymmetric hurricane model by Emanuel (1986).

Throughout much of the troposphere, θ_e has a negative radial gradient. This is, in part, a reflection of the structure in the boundary layer. Below about 600 m, the negative radial gradient of θ_e is apparent only inside a radius of about 100 km and is a result of the presumed increase in surface moisture flux with decreasing radius (Malkus and Riehl 1960, Ooyama 1969). Such a localized gradient was documented in the classical observational analysis of Hawkins and Imbombo (1976) and has been confirmed by more recent work (Montgomery *et al.* 2006, Marks *et al.* 2008, Bell and Montgomery 2008, Smith and Montgomery 2013). Maximum values of θ_e exceed 355 K in the low to mid troposphere near and inside the inner eyewall region. The near surface value is approximately constant at 350 K outside of 100 km radius. The minimum value in the mid to low troposphere falls to values less than 320 K beyond about 300 km radius (the region highlighted in blue in Figure 1d).

3.4. Relative humidity

Values of relative humidity[§], (RH , panel (d)), exceed 90% inside a radius of 200 km and below about 7 km altitude. At larger radii, values remain relatively high (> 80%) in a shallow near-surface layer, but decrease markedly with height with values of less than 50% through much of the troposphere, especially beyond a radius of about 300 km. These low values are an indication of drying in the subsiding branch of the secondary circulation. The RH starts to drop off beyond the outer wind maximum, perhaps suggesting that this wind maximum either forms near the boundary with dry air or acts as a potential barrier to dry air. Comparison with Figure 1c shows that relatively dry air is being drawn inwards just below the outflow layer.

4. Conclusions

In this paper we have used a dropsonde data set with unprecedentedly high spatial coverage from the NASA HS3 experiment to analyze the azimuthally-averaged structure of Hurricane Edouard (2014) just after its peak intensity. The dropsondes were deployed from above the tropopause and enable a sampling of the full troposphere. The analyses of these unique observations confirm many known structural features of a mature tropical cyclone, e.g. tangential wind structure, radial wind structure (low-level inflow in a shallow boundary layer, outflow in the upper troposphere), warm core temperature structure, relative humidity structure and equivalent potential temperature structure.

Nevertheless, even with such an unprecedentedly high density of dropsondes to estimate the azimuthally averaged structure, there remain issues in reconciling the radial and tangential structure of the hurricane in the upper troposphere. One issue appears to arise from the analysis assumption of a quasi-steady state during the period of observations, an assumption that stands out as an important limitation of any analysis of dropsonde data over such an extended period of observations as the one in this case. Another issue is that details of the analyzed radial velocity field are somewhat sensitive to the way in which the dropsonde data are partitioned to produce an azimuthal average.

5. Acknowledgements

We thank Jun Zhang and two anonymous reviewers for their perceptive and constructive comments on the original manuscript. RKS acknowledges financial support for tropical cyclone research from the Office of Naval Research Global under Grant No. N62909-15-1-N021. MTM acknowledges the support of NSF grant AGS-1313948, NOAA HFIP grant N0017315WR00048, NASA (HS3) grant NNG11PK021, ONR grant N0001417WX00336, and the U. S. Naval Postgraduate School.

[‡]The quantity θ_e is calculated using Bolton's formula (Bolton, 1980, Equation (43)).

[§]The relative humidity is calculated relative to water saturation.

6. References

- Abarca SF, Montgomery MT, Braun SA, Dunion J. 2016. On the secondary eyewall formation of Hurricane Edouard (2014). *Mon. Weather Rev.*, **144**: 3321-3331.
- Bell MM, Montgomery MT. 2008. Observed structure, evolution, and potential intensity of Category 5 Hurricane Isabel (2003) from 12 to 14 September. *Mon. Weather Rev.*, **65**: 2025-2046.
- Bolton D. 1980. The computation of equivalent potential temperature. *Mon. Weather Rev.*, **108**: 1046-053.
- Braun SA and Coauthors, 2013: NASAs Genesis and Rapid Intensification Processes (GRIP) field experiment. *Bull. Amer. Meteor. Soc.*, **94**: 345-363.
- Braun, SA, Newman PA, Heymsfield GM. 2016. NASAs Hurricane and Severe Storm Sentinel (HS3) investigation. *Bull. Amer. Meteor. Soc.*, **97**: 2085-2102.
- Emanuel KA, 1986. An air-sea interaction theory for tropical cyclones. Part I: steady state maintenance. *J. Atmos. Sci.*, **43**: 585-604.
- Hawkins HF, Rubsam DT. 1968: Hurricane Hilda, 1964. II: Structure and budgets of the hurricane on October 1, 1964. *Mon. Weather Rev.*, **96**: 617-636.
- Hawkins HF, Imbembo SM. 1976. The structure of a small, intense Hurricane Inez 1966. *Mon. Weather Rev.*, **104**: 418-442.
- Kilroy G, Smith RK, Montgomery MT. 2016. Why do model tropical cyclones grow progressively in size and decay in intensity after reaching maturity? *J. Atmos. Sci.*, **73**: 487-503.
- La Seur NE, Hawkins HF. 1963. An analysis of Hurricane Cleo (1958) based on data from research reconnaissance aircraft. *Mon. Weather Rev.*, **91**: 694-709.
- Malkus JS, Riehl H. 1960. On the dynamics and energy transformations in steady-state hurricanes. *Tellus*, **12**: 1-19.
- Marks FD, Black PG, Montgomery MT, Burpee RW. 2008. Structure of the eye and eyewall of Hurricane Hugo (1989). *Mon. Weather Rev.*, **136**: 1237-1259.
- Montgomery MT, Smith RK. 2017. Recent developments in the fluid dynamics of tropical cyclones. *Annu. Rev. Fluid Mech.*, **49**: 1-33.
- Montgomery MT, Bell MM, Abernethy SD, Black ML. 2006: Hurricane Isabel (2003): New insights into the physics of intense storms. Part I. Mean vortex structure and maximum intensity estimates. *Bull. Amer. Meteor. Soc.*, **87**: 1335-1347.
- Montgomery MT, Kilroy G, Smith RK, Črnivec N. 2018b. Tropical cyclone life cycle in a three-dimensional numerical simulation: Part II: Unbalanced and nonaxisymmetric dynamical processes. *Q. J. R. Meteorol. Soc.*, **144**: submitted.
- Munsell EB, Zhang F, Braun SA, Sippel JA, Didlake AC. 2018. The inner-core temperature structure of Hurricane Edouard (2014): Observations and ensemble variability. *Mon. Weather Rev.*, **91**: 135-155.
- Ooyama K. 1969. Numerical simulation of the life-cycle of tropical cyclones. *J. Atmos. Sci.*, **26**: 3-40.
- Persing J, Montgomery MT, McWilliams J, Smith, RK. 2013. Asymmetric and axisymmetric dynamics of tropical cyclones. *Atmos. Chem. Phys.*, **13**, 12299-12341.
- Rayleigh JWS. 1916. On the dynamics of revolving fluids. *Proc. Roy. Soc. A*, **93**, 148 (also Sci. Papers, 6, 447).
- Rotunno R, Emanuel KA. 1987. An air-sea interaction theory for tropical cyclones. Part II Evolutionary study using a nonhydrostatic axisymmetric numerical model. *J. Atmos. Sci.*, **44**: 542-561.
- Smith RK, Montgomery MT. 2013. How important is the isothermal expansion effect to elevating equivalent potential temperature in the hurricane inner-core? *Q. J. R. Meteorol. Soc.*, **138**: 1-5.
- Smith RK, Montgomery MT, Persing J. 2014. On steady-state tropical cyclones. *Q. J. R. Meteorol. Soc.*, **140**: 2638-2649.
- Schmidt C, Smith RK. 2016. Tropical cyclone evolution in a minimal axisymmetric model revisited. *Q. J. R. Meteorol. Soc.*, **142**: 1505-1516.
- Stewart, S. R., 2014: National Hurricane Center Tropical Cyclone Report: Hurricane Edouard (1119 September 2014). Tropical Cyclone Rep. AL062014, National Hurricane Center, 19pp. Available online at http://www.nhc.noaa.gov/data/tcr/AL062014_Edouard.pdf.
- Young K *et al.* 2016. Hurricane and Severe Storm Sentinel (HS3) 2014 Global Hawk Dropsonde Data Analysis Summary. <http://data.eol.ucar.edu/datafile/nph-get/348.004/readme.V3.HS3-2014.GHdropsonde.pdf>
- Wick, G., 2015: Hurricane and Severe Storm Sentinel (HS3) Global Hawk AVAPS Dropsonde System. NASA Global Hydrology Resource Center DAAC, doi:<https://doi.org/10.5067/H3/AVAPS/DROPSONDE/DATA201>.
- Zawislak J, Jiang H, Alvey GR, Zipser EJ, Rogers RF, Zhang JA, Stevenson SN. 2016. Observations of the structure and evolution of Hurricane Edouard (2014) during intensity change. Part I: Relationship between the thermodynamic structure and precipitation. *Mon. Weather Rev.*, **144**: 3333-3354.



Azimuthally-averaged structure of Hurricane Edouard (2014) just after peak intensity

Roger K. Smith^{a*}, Michael T. Montgomery^b and Scott Braun^c

^a *Meteorological Institute, Ludwig Maximilians University of Munich, Munich, Germany*

^b *Dept. of Meteorology, Naval Postgraduate School, Monterey, CA, USA*

^c *Laboratory for Mesoscale Atmospheric Processes, NASA Goddard Space Flight Center, Greenbelt, Maryland, MD, USA*

*Correspondence to: Prof. Roger K. Smith, Meteorological Institute, Ludwig-Maximilians University of Munich, Theresienstr. 37, 80333 Munich, Germany. E-mail: roger.smith@lmu.de

Analyses of dropsonde data collected in Hurricane Edouard (2014) just after its mature stage are presented. These data, have unprecedentedly high spatial resolution, based on 87 dropsondes released by the unmanned NASA Global Hawk from an altitude of 18 km during the Hurricane and Severe Storm Sentinel (HS3) field campaign. Attempts are made to relate the analyses of the data to theories of tropical cyclone structure and behaviour. The tangential wind and thermal fields show the classical structure of a warm core vortex, in this case with a secondary eyewall feature. The equivalent potential temperature (θ_e) field shows also the expected structure with a mid-tropospheric minimum at outer radii and contours of θ_e flaring upwards and outwards at inner radii and, with some imagination, roughly congruent to the surfaces of absolute angular momentum. However, details of the analysed radial velocity field are somewhat sensitive to the way in which the sonde data are partitioned to produce an azimuthal average. This sensitivity is compounded by an apparent limitation of the assumed steadiness of the storm over the period of data collection.

Key Words: Tropical cyclone, hurricane, observed structure and behaviour

Received November 9, 2018; Revised ; Accepted

1. Introduction

In the past there have been few measurements of hurricane structure through the depth of the troposphere, the reason being that most aircraft reconnaissance flights have not been able to sample the upper troposphere. Some classic observational studies are those of La Seur and Hawkins (1963), Hawkins and Rubsam (1968) and Hawkins and Imbembo (1976) to whom *in situ* data from an instrumented high-flying jet aircraft were available. The situation changed recently through the deployment of the NASA* Global Hawk, an unmanned drone capable of releasing dropsondes in rapid succession from the lower stratosphere. During NASA's Hurricane and Severe Storm Sentinel (HS3; Braun *et al.* 2016) field campaign in 2014, comparatively high temporal and spatial resolution dropsonde observations were made over the Atlantic Ocean in Hurricane Edouard during four missions between 11 to 19 September 2014. A map showing the location of each dropsonde is contained in Figure 1 of Zawislak *et al.* (2016), while a description of the storm during its lifetime is given by Stewart (2014). Brief descriptions of the storm and the missions flown was given by Braun *et al.* (2016) and Munsell *et al.* (2018).

The structure of Edouard was particularly well sampled on 16-17 September while it was near peak intensity. On this mission, which lasted about 23 h, 87 dropsondes were deployed into the hurricane from a height of 18 km. The purpose of this paper is to present azimuthally averaged, radius-height cross sections of various quantities obtained from analyses of these unique data and to compare these analyses with theories of tropical cyclone behaviour.

2. Data

The 87 dropsondes were released into Edouard between 15:06 UTC 16 September and 08:28 UTC 17 September 2014 during which time the storm moved from about 32 N to 35 N (Stewart 2014, Table 1). The distribution of the dropsondes is shown in Abarca *et al.*

*National Atmospheric and Space Administration

(2016, Figure 2(a)). The sonde data were post-processed by NCAR (see Wick *et al.* 2015) using their Atmospheric Sounding Processing Environment (ASPEN) software (Young *et al.* 2016). The original analyses of the dropsondes did not include a dry bias correction in the upper troposphere, but the present ones have used the correct humidity values. The analysis of these sondes is described briefly below.

2.1. Computation of azimuthal averages

To calculate the azimuthal averages, the dropsonde data were first interpolated to 181 pressure levels with a spacing of 5 mb. The storm centre positions over the time period of the flight were used to determine the location of each dropsonde relative to the evolving centre position. The National Hurricane Center best track data were used also to estimate the mean storm motion over the flight period. The positions of the dropsonde data were shifted to a reference time of 00 UTC 17 September using the storm motion and the time difference between the sonde time and this reference time. Here, the sonde time is the time of the actual measurement at a particular level. Using these adjusted positions relative to the centre, radial and tangential velocities were calculated with the storm motion removed to obtain storm-relative flow. This analysis was done for all dropsondes during the flight. Bins were then created for averaging after all derived fields such as radial and tangential velocity were calculated.

The midpoints of the bins were at radial locations 10, 30, 50, 70, 100, 150, 210, 270, 330, 400, 480, and 560 km from the centre[†]. The number of soundings were distributed within each bin as follows: 0-20 km radius (11 sondes), 20-40 km (9), 40-60 km (6), 60-80 km (7), 80-120 km (10), 120-180 km (0), 180-240 km (9), 240-300 km (8), 300-360 km (8), 360-440 km (4), 440-520 km (8), 520-600 km (7). No additional smoothing was applied to the individual dropsonde data. If, when computing the azimuthal mean, some values were missing from individual soundings, they were simply not included in the calculation of the mean. Because there were no dropsonde data at radii between 120 km and 200 km and therefore in the radial bin 120-180 km, the azimuthal values for 150 km radius were determined by linear interpolation between the bin midpoints at 100 km and 210 km.

2.2. Steady-state composite data

Although the storm was at peak intensity near the start of measurements, the intensity decreased by about 10 m s^{-1} during the period of measurements (see Abarca *et al.* 2016, Figure 1 and accompanying discussion of the various factors in this decay). Because of the relatively long period of data collection, attempts were made to subdivide the data into two separate subsets, one in the first half of the flight and another in the second half. In this subdivision the number of soundings were distributed as follows over the course of the first half of the flight, and the second half of the flight: radius 0-20 km (first half 6, second half 5), 20-40 km (4, 5), 40-60 km (3, 3), 60-80 km (3, 4), 80-120 km (5, 5), 120-180 km (0, 0), 180-240 km (4, 5), 240-300 km (4,4), 300-360 km (3, 5), 360-440 km (1, 3), 440-520 km (3, 5), 520-600 km (2,5). Clearly, breaking up the soundings into two separate halves of the flight reduces the number of samples in each radial bin, although not necessarily by half since a good part of the first half of the flight was sampling storm outflow beyond 600 km radius. As mentioned earlier, the biggest problem occurs between 120-180 km, where there are no soundings for either time. For these reasons, and because there was qualitative similarity between the derived structures from the two data sets in regions where there was data, we have based the analysis below on a composite for the whole period. Thus, all the storm-relative dropsonde data from the whole flight occurring within a particular bin were averaged. This procedure is tantamount to assuming the storm to be in a quasi-steady state for the duration of the flight. Some limitations of the quasi-steady state assumption will emerge later.

3. Storm structure

Figure 1 shows radius-height cross sections obtained from the dropsonde data as described in subsection 2.1 above. The wind data are smoothed using a centred 1-4-1 box filter applied 10 times.

3.1. Tangential wind and warm core structure

The storm-relative composite tangential wind component (v , Figure 1a) and temperature perturbation (dT , panel (b)) show the classical structure of a warm-cored vortex with the maximum wind in the lower troposphere and the wind decreasing with height, becoming anticyclonic in the upper troposphere. The decrease in the tangential velocity component with height corresponds through balance considerations with the warm-core structure (see Figure 1b).

There is evidence of a weak inner tangential wind maximum near 40 km and an outer maximum at a radius of about 100 km. The formation of the outer wind maximum was the focus of a separate study by Abarca *et al.* (2016). The upper-level anticyclone begins at a radius of about 80 km, while the strength of the anticyclone increases with radius and the anticyclonic circulation deepens with increasing radius. The maximum anticyclonic flow is found at an altitude between 14 and 15 km at 500 km radius and is clearly increasing beyond this radius.

Figure 1(a) shows also the absolute angular momentum (or M -) surfaces corresponding with the tangential wind component. These are calculated using the formula $M = rv + \frac{1}{2}fr^2$, where r is the radius and f is the Coriolis parameter at the mean latitude of Edouard (33°N) during the period of dropsonde measurements. Consistent with theoretical expectations, the M -surfaces flare outwards with height, with M mostly increasing with radius and decreasing with height. There is a local maximum of M , located at a height of about 6 km and a radius of just over 400 km. This maximum is accompanied by a negative radial gradient of M at radii beyond it, implying that, according to linear theory, the flow would be centrifugally unstable locally (Rayleigh, 1916). Since the dropsonde data at these radii are rather sparse (see Abarca *et al.* 2016, Figure 3(b)) and the period of collection spans an interval of more than 16 h, we do not attribute much significance to the implied regions of instability at these radii.

[†]The data set is the same as that used by Abarca *et al.* (2016). However, the subdivision into bins is somewhat different. Even so, the tangential wind field in Abarca *et al.* (Figure 3(a)) is very similar to that shown in Figure 1(a). The pressure field is rather smooth and should be similar between the two analyses. Indeed, Abarca *et al.* did note that “the data were robust to different bin-length choices”.

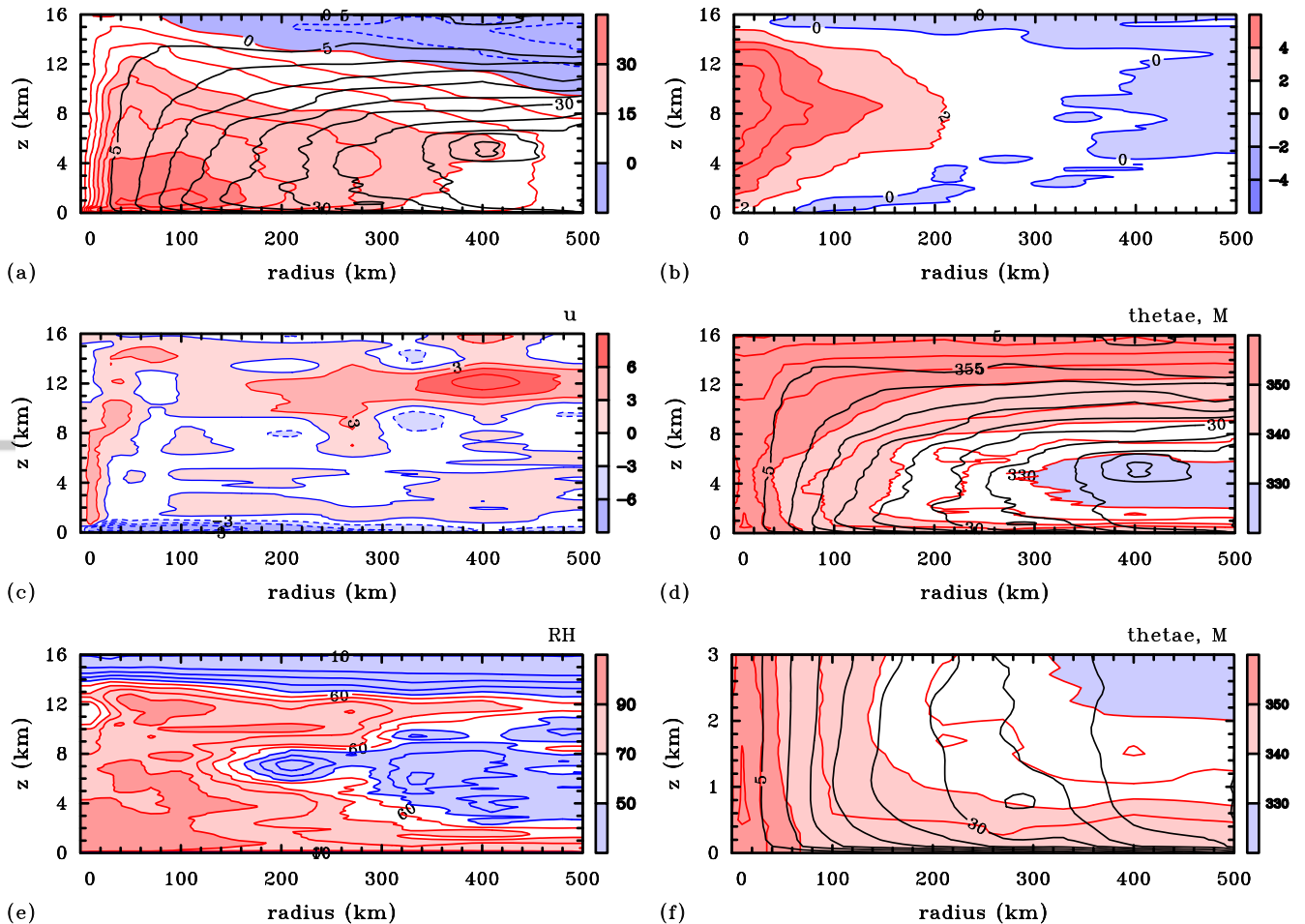


Figure 1. Radius-height cross sections of selected fields derived from the dropsonde data: (a) tangential velocity component, contour interval 5 m s^{-1} , shading indicated on the side bar in m s^{-1} , and absolute angular momentum, black lines, contour interval $5 \times 10^5 \text{ m}^2 \text{ s}^{-1}$; (b) temperature perturbation, contour interval 2 K (positive values), 1 K (negative values), shading indicated on the side bar in K; (c) radial velocity component, contour interval 3 m s^{-1} , shading indicated on the side bar in m s^{-1} ; (d) equivalent potential temperature, contour interval 10 K, shading indicated on the side bar in K, and absolute angular momentum, black lines, contours as in (a); (e) relative humidity, contour interval 10%, shading indicated on the side bar in %; (f) a zoomed in version of panel (d) at heights below 3 km.

There is a marked ($> 2^\circ\text{C}$) positive temperature anomaly inside a radius of about 200 km (Figure 1(b)). This anomaly has a maximum of nearly 10°C on the axis of rotation at an altitude of about 8 km. (For the calculation of temperature perturbation, the “environmental temperature” was determined by averaging all dropsonde data at radii > 200 km. Specifically, there were 46 soundings used in calculation of the “environmental” mean temperature for the temperature perturbation plot.) There is a weak cold temperature anomaly at low levels beyond about 60 km radius. The negative temperature anomalies beyond about 400 km radius and those above 13 km are due to the way the ambient temperature has been defined and are presumably not significant. Since the reference temperature is based on an average of all soundings beyond a radius of 200 km and if the temperature in this region decreases outwards, negative anomalies would be expected at large radii. The low-level negative anomaly between 60 and 240 km radius is plausibly a result of the evaporation of falling raindrops.

3.2. Radial velocity component

The storm-relative composite radial flow (u , Figure 1c) shows two features of the classical tropical cyclone structure with a layer of strong inflow below about 1 km extending to large radii as well as a layer of strong outflow in the upper troposphere between about 9 and 14 km depending on radius. The maximum low-level inflow is about 15 m s^{-1} . The layer of upper tropospheric outflow is a few km deep with a maximum of nearly 12 m s^{-1} at about 12 km altitude and 400 km radius.

Perhaps surprisingly, the level of maximum outflow in the upper troposphere does not coincide with that of the maximum anticyclonic flow, which is typically 2 km higher. A plausible explanation for this finding is that during the earlier period of measurement, the outflow was higher than during the later part. This possibility is supported by the fact that there are two layers of outflow, one centred around 14 km height, emanating from the inner eyewall and another, centred around 12 km height, emanating from the outer eyewall (see Abarca *et al.* 2016 for further details of the double eyewall structure). The upper layer has its maximum well within a radius of 100 km, whereas the lower maximum, which is much stronger, occurs at a radius of 400 km. The foregoing issue in reconciling the radial and tangential wind structure in the upper troposphere highlights a potential limitation of assuming that the storm is in a quasi-steady state for the purpose of the analysis.

In the lower troposphere there are significant regions of outflow above the shallow surface-based boundary layer inflow. This outflow has a local maximum in the inner eyewall (near 20 km radius) and has a layered structure beyond a radius of about 90 km starting near outer eyewall. This pattern of outflow would suggest that the flow in these regions is spinning down by the outward radial advection of the M -surfaces. However, this spin down effect would be countered by the vertical advection of air with high values of M from the boundary layer, at least in the inner core region. In this context, it was shown by Abarca *et al.* (2016, see their Figure 4b), that the

boundary layer flow was supergradient below both the primary and secondary eyewalls on the day prior to the present observations. The fact that the storm had just begun to weaken (see section 2.1) would indicate that the spin down tendency due to the outward radial advection of the M -surfaces would be dominant, at least for the inner eyewall. The role of the vertical advection of supergradient values of M from the boundary layer to spin up the inner eyewall was highlighted by the study of Schmidt and Smith (2016) using a minimal three-layer numerical model and was discussed in a more general context by Montgomery and Smith (2017: section 3.9).

Beyond about 300 km radius in Figure 1c, where the boundary layer flow is typically subgradient, there is mostly outflow in the lower troposphere above the boundary layer. At such radii, this outflow would carry the M surfaces outwards leading to a spin-down of the tangential winds and therefore a contracting in the storm size (see Kilroy *et al.* 2016 for a discussion of the factors influencing storm size).

Other interesting features of the radial flow are the layers of inflow in the upper troposphere, above and below the two outflow layers. Such features are often seen in numerical model simulations (e.g. Rotunno and Emanuel 1987, Figure 5c; Persing *et al.* 2013, Figures 10a, 11a, 15a; Montgomery *et al.* 2018, Figures 7b, 8b), but to our knowledge are not well understood.

It should be pointed out that while the broad features of the analyzed radial flow field are robust (e.g. the strong inflow in the boundary layer, the upper-level outflow and the outflow in the inner and outer eyewalls), the details of this field are somewhat sensitive to the way in which the sonde data are binned to produce an azimuthal average (not shown). This sensitivity is compounded by an apparent limitation of the assumed steadiness of the storm over the period of data collection discussed above.

3.3. Pseudo-equivalent potential temperature

The distribution of pseudo-equivalent potential temperature[‡], θ_e , (Figure 1d and 1f) shows the classical structure also. (Figure 1f is a zoomed in plot of Figure 1d in the lowest 3 km.) Principal features are: the mid-tropospheric minimum beyond a radius of about 100 km, increasing in prominence with radius; the tendency for the isopleths of θ_e to become close to vertical in the lower troposphere inside a radius of 100 km; and the tendency for the isopleths of θ_e to slope outwards and become close to horizontal in the upper tropospheric outflow layer. With a little imagination, there is an approximate congruence between the θ_e - and M -surfaces in the inner core region and in the upper troposphere, at least out to 250 km radius (the M -surfaces are shown also in Figure 1d and 1f). This approximate congruence forms the cornerstone of the steady-state axisymmetric hurricane model by Emanuel (1986).

Throughout much of the troposphere, θ_e has a negative radial gradient. This is, in part, a reflection of the structure in the boundary layer. Below about 600 m, the negative radial gradient of θ_e is apparent only inside a radius of about 100 km and is a result of the presumed increase in surface moisture flux with decreasing radius (Malkus and Riehl 1960, Ooyama 1969). Such a localized gradient was documented in the classical observational analysis of Hawkins and Imbombo (1976) and has been confirmed by more recent work (Montgomery *et al.* 2006, Marks *et al.* 2008, Bell and Montgomery 2008, Smith and Montgomery 2013). Maximum values of θ_e exceed 355 K in the low to mid troposphere near and inside the inner eyewall region. The near surface value is approximately constant at 350 K outside of 100 km radius. The minimum value in the mid to low troposphere falls to values less than 320 K beyond about 300 km radius (the region highlighted in blue in Figure 1d).

3.4. Relative humidity

Values of relative humidity[§], (RH , panel (d)), exceed 90% inside a radius of 200 km and below about 7 km altitude. At larger radii, values remain relatively high (> 80%) in a shallow near-surface layer, but decrease markedly with height with values of less than 50% through much of the troposphere, especially beyond a radius of about 300 km. These low values are an indication of drying in the subsiding branch of the secondary circulation. The RH starts to drop off beyond the outer wind maximum, perhaps suggesting that this wind maximum either forms near the boundary with dry air or acts as a potential barrier to dry air. Comparison with Figure 1c shows that relatively dry air is being drawn inwards just below the outflow layer.

4. Conclusions

In this paper we have used a dropsonde data set with unprecedentedly high spatial coverage from the NASA HS3 experiment to analyze the azimuthally-averaged structure of Hurricane Edouard (2014) just after its peak intensity. The dropsondes were deployed from above the tropopause and enable a sampling of the full troposphere. The analyses of these unique observations confirm many known structural features of a mature tropical cyclone, e.g. tangential wind structure, radial wind structure (low-level inflow in a shallow boundary layer, outflow in the upper troposphere), warm core temperature structure, relative humidity structure and equivalent potential temperature structure.

Nevertheless, even with such an unprecedentedly high density of dropsondes to estimate the azimuthally averaged structure, there remain issues in reconciling the radial and tangential structure of the hurricane in the upper troposphere. One issue appears to arise from the analysis assumption of a quasi-steady state during the period of observations, an assumption that stands out as an important limitation of any analysis of dropsonde data over such an extended period of observations as the one in this case. Another issue is that details of the analyzed radial velocity field are somewhat sensitive to the way in which the dropsonde data are partitioned to produce an azimuthal average.

5. Acknowledgements

We thank Jun Zhang and two anonymous reviewers for their perceptive and constructive comments on the original manuscript. RKS acknowledges financial support for tropical cyclone research from the Office of Naval Research Global under Grant No. N62909-15-1-N021. MTM acknowledges the support of NSF grant AGS-1313948, NOAA HFIP grant N0017315WR00048, NASA (HS3) grant NNG11PK021, ONR grant N0001417WX00336, and the U. S. Naval Postgraduate School.

[‡]The quantity θ_e is calculated using Bolton's formula (Bolton, 1980, Equation (43)).

[§]The relative humidity is calculated relative to water saturation.

6. References

- Abarca SF, Montgomery MT, Braun SA, Dunion J. 2016. On the secondary eyewall formation of Hurricane Edouard (2014). *Mon. Weather Rev.*, **144**: 3321-3331.
- Bell MM, Montgomery MT. 2008. Observed structure, evolution, and potential intensity of Category 5 Hurricane Isabel (2003) from 12 to 14 September. *Mon. Weather Rev.*, **65**: 2025-2046.
- Bolton D. 1980. The computation of equivalent potential temperature. *Mon. Weather Rev.*, **108**: 1046-053.
- Braun SA and Coauthors, 2013: NASAs Genesis and Rapid Intensification Processes (GRIP) field experiment. *Bull. Amer. Meteor. Soc.*, **94**: 345-363.
- Braun, SA, Newman PA, Heymsfield GM. 2016. NASAs Hurricane and Severe Storm Sentinel (HS3) investigation. *Bull. Amer. Meteor. Soc.*, **97**: 2085-2102.
- Emanuel KA, 1986. An air-sea interaction theory for tropical cyclones. Part I: steady state maintenance. *J. Atmos. Sci.*, **43**: 585-604.
- Hawkins HF, Rubsam DT. 1968: Hurricane Hilda, 1964. II: Structure and budgets of the hurricane on October 1, 1964. *Mon. Weather Rev.*, **96**: 617-636.
- Hawkins HF, Imbembo SM. 1976. The structure of a small, intense Hurricane Inez 1966. *Mon. Weather Rev.*, **104**: 418-442.
- Kilroy G, Smith RK, Montgomery MT. 2016. Why do model tropical cyclones grow progressively in size and decay in intensity after reaching maturity? *J. Atmos. Sci.*, **73**: 487-503.
- La Seur NE, Hawkins HF. 1963. An analysis of Hurricane Cleo (1958) based on data from research reconnaissance aircraft. *Mon. Weather Rev.*, **91**: 694-709.
- Malkus JS, Riehl H. 1960. On the dynamics and energy transformations in steady-state hurricanes. *Tellus*, **12**: 1-19.
- Marks FD, Black PG, Montgomery MT, Burpee RW. 2008. Structure of the eye and eyewall of Hurricane Hugo (1989). *Mon. Weather Rev.*, **136**: 1237-1259.
- Montgomery MT, Smith RK. 2017. Recent developments in the fluid dynamics of tropical cyclones. *Annu. Rev. Fluid Mech.*, **49**: 1-33.
- Montgomery MT, Bell MM, Abernethy SD, Black ML. 2006: Hurricane Isabel (2003): New insights into the physics of intense storms. Part I. Mean vortex structure and maximum intensity estimates. *Bull. Amer. Meteor. Soc.*, **87**: 1335-1347.
- Montgomery MT, Kilroy G, Smith RK, Črnivec N. 2018b. Tropical cyclone life cycle in a three-dimensional numerical simulation: Part II: Unbalanced and nonaxisymmetric dynamical processes. *Q. J. R. Meteorol. Soc.*, **144**: submitted.
- Munsell EB, Zhang F, Braun SA, Sippel JA, Didlake AC. 2018. The inner-core temperature structure of Hurricane Edouard (2014): Observations and ensemble variability. *Mon. Weather Rev.*, **91**: 135-155.
- Ooyama K. 1969. Numerical simulation of the life-cycle of tropical cyclones. *J. Atmos. Sci.*, **26**: 3-40.
- Persing J, Montgomery MT, McWilliams J, Smith, RK. 2013. Asymmetric and axisymmetric dynamics of tropical cyclones. *Atmos. Chem. Phys.*, **13**, 12299-12341.
- Rayleigh JWS. 1916. On the dynamics of revolving fluids. *Proc. Roy. Soc. A*, **93**, 148 (also Sci. Papers, 6, 447).
- Rotunno R, Emanuel KA. 1987. An air-sea interaction theory for tropical cyclones. Part II Evolutionary study using a nonhydrostatic axisymmetric numerical model. *J. Atmos. Sci.*, **44**: 542-561.
- Smith RK, Montgomery MT. 2013. How important is the isothermal expansion effect to elevating equivalent potential temperature in the hurricane inner-core? *Q. J. R. Meteorol. Soc.*, **138**: 1-5.
- Smith RK, Montgomery MT, Persing J. 2014. On steady-state tropical cyclones. *Q. J. R. Meteorol. Soc.*, **140**: 2638-2649.
- Schmidt C, Smith RK. 2016. Tropical cyclone evolution in a minimal axisymmetric model revisited. *Q. J. R. Meteorol. Soc.*, **142**: 1505-1516.
- Stewart, S. R., 2014: National Hurricane Center Tropical Cyclone Report: Hurricane Edouard (1119 September 2014). Tropical Cyclone Rep. AL062014, National Hurricane Center, 19pp. Available online at http://www.nhc.noaa.gov/data/tcr/AL062014_Edouard.pdf.
- Young K *et al.* 2016. Hurricane and Severe Storm Sentinel (HS3) 2014 Global Hawk Dropsonde Data Analysis Summary. <http://data.eol.ucar.edu/datafile/nph-get/348.004/readme.V3.HS3-2014.GHdropsonde.pdf>
- Wick, G., 2015: Hurricane and Severe Storm Sentinel (HS3) Global Hawk AVAPS Dropsonde System. NASA Global Hydrology Resource Center DAAC, doi:<https://doi.org/10.5067/H3/AVAPS/DROPSONDE/DATA201>.
- Zawislak J, Jiang H, Alvey GR, Zipser EJ, Rogers RF, Zhang JA, Stevenson SN. 2016. Observations of the structure and evolution of Hurricane Edouard (2014) during intensity change. Part I: Relationship between the thermodynamic structure and precipitation. *Mon. Weather Rev.*, **144**: 3333-3354.

References

- Abarca SF, Montgomery MT, Braun SA, Dunion J. 2016. On the secondary eyewall formation of Hurricane Edouard (2014). *Mon. Weather Rev.*, **144**: 3321-3331.
- Bell MM, Montgomery MT. 2008. Observed structure, evolution, and potential intensity of Category 5 Hurricane Isabel (2003) from 12 to 14 September. *Mon. Weather Rev.*, **65**: 2025-2046.
- Bolton D. 1980. The computation of equivalent potential temperature. *Mon. Weather Rev.*, **108**: 1046-1053.
- Braun SA and Coauthors, 2013: NASA's Genesis and Rapid Intensification Processes (GRIP) field experiment. *Bull. Amer. Meteor. Soc.*, **94**: 345-363.
- Braun, SA, Newman PA, Heysfield GM. 2016. NASA's Hurricane and Severe Storm Sentinel (HS3) investigation. *Bull. Amer. Meteor. Soc.*, **97**: 2085-2102.
- Emanuel KA, 1986. An air-sea interaction theory for tropical cyclones. Part I: steady state maintenance. *J. Atmos. Sci.*, **43**: 585-604.
- Hawkins HF, Rubsam DT. 1968: Hurricane Hilda, 1964. II: Structure and budgets of the hurricane on October 1, 1964. *Mon. Weather Rev.*, **96**: 617-636.
- Hawkins HF, Imbembo SM. 1976. The structure of a small, intense Hurricane Inez 1966. *Mon. Weather Rev.*, **104**: 418-442.
- Kilroy G, Smith RK, Montgomery MT. 2016. Why do model tropical cyclones grow progressively in size and decay in intensity after reaching maturity? *J. Atmos. Sci.*, **73**: 487-503.

- La Seur NE, Hawkins HF. 1963. An analysis of Hurricane Cleo (1958) based on data from research reconnaissance aircraft. *Mon. Weather Rev.*, **91**: 694-709.
- Malkus JS, Riehl H. 1960. On the dynamics and energy transformations in steady-state hurricanes. *Tellus*, **12**: 1-19.
- Marks FD, Black PG, Montgomery MT, Burpee RW. 2008. Structure of the eye and eyewall of Hurricane Hugo (1989). *Mon. Weather Rev.*, **136**: 1237-1259.
- Montgomery MT, Smith RK. 2017. Recent developments in the fluid dynamics of tropical cyclones. *Annu. Rev. Fluid Mech.*, **49**: 1-33.
- Montgomery MT, Bell MM, Abernethy SD, Black ML. 2006. Hurricane Isabel (2003): New insights into the physics of intense storms. Part I. Mean vortex structure and maximum intensity estimates. *Bull. Amer. Meteor. Soc.*, **87**: 1335-1347.
- Montgomery MT, Kilroy G, Smith RK, Črnivec N. 2018. Tropical cyclone life cycle in a three-dimensional numerical simulation: Part II: Unbalanced and nonaxisymmetric dynamical processes. *Q. J. R. Meteorol. Soc.*, **144**: submitted.
- Munsell EB, Zhang F, Braun SA, Sippel JA, Didlake AC. 2018. The inner-core temperature structure of Hurricane Edouard (2014): Observations and ensemble variability. *Mon. Weather Rev.*, **91**: 135-155.
- Ooyama K. 1969. Numerical simulation of the life-cycle of tropical cyclones. *J. Atmos. Sci.*, **26**: 3-40.
- Persing J, Montgomery MT, McWilliams J, Smith, RK. 2013. Asymmetric and axisymmetric dynamics of tropical cyclones. *Atmos. Chem. Phys.*, **13**, 12299-12341.
- Rayleigh JWS. 1916. On the dynamics of revolving fluids. *Proc. Roy. Soc. A*, **93**, 148 (also *Sci. Papers*, 6, 447).

- Rotunno R, Emanuel KA. 1987. An air-sea interaction theory for tropical cyclones. Part II Evolutionary study using a nonhydrostatic axisymmetric numerical model. *J. Atmos. Sci.*, **44**: 542-561.
- Smith RK, Montgomery MT. 2013. How important is the isothermal expansion effect to elevating equivalent potential temperature in the hurricane inner-core? *Q. J. R. Meteorol. Soc.*, **138**: 1-5.
- Smith RK, Montgomery MT, Persing J. 2014. On steady-state tropical cyclones. *Q. J. R. Meteorol. Soc.*, **140**: 2638-2649.
- Schmidt C, Smith RK. 2016. Tropical cyclone evolution in a minimal axisymmetric model revisited. *Q. J. R. Meteorol. Soc.*, **142**: 1505-1516.
- Stewart, S. R., 2014: National Hurricane Center Tropical Cyclone Report: Hurricane Edouard (1119 September 2014). Tropical Cyclone Rep. AL062014, National Hurricane Center, 19pp. Available online at http://www.nhc.noaa.gov/data/tcr/AL062014_Edouard.pdf.
- Young K *et al.* 2016. Hurricane and Severe Storm Sentinel (HS3) 2014 Global Hawk Dropsonde Data Analysis Summary. <http://data.eol.ucar.edu/datafile/nph-get/348.004/readme.V3.HS3-2014.GHdropsonde.pdf>
- Wick, G., 2015: Hurricane and Severe Storm Sentinel (HS3) Global Hawk AVAPS Dropsonde System. NASA Global Hydrology Resource Center DAAC, doi:<https://doi.org/10.5067/-HS3/AVAPS/DROPSONDE/DATA201>.
- Zawislak J, Jiang H, Alvey GR, Zipser EJ, Rogers RF, Zhang JA, Stevenson SN. 2016. Observations of the structure and evolution of Hurricane Edouard (2014) during intensity change. Part I: Relationship between the thermodynamic structure and precipitation. *Mon. Weather Rev.*, **144**: 3333-3354.